J. Fluid Mech. (2024), *vol*. 997, A59, doi:10.1017/jfm.2024.582

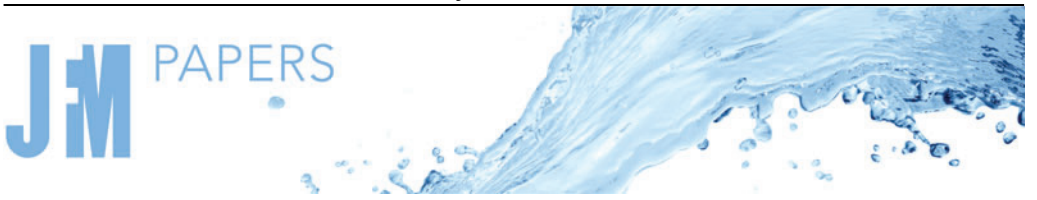

Harnessing wall slip towards tunable microswimming in Poiseuille flow

Soumyajit Ghosh[1], **Srimoyee Ghoshal**[2] **and Antarip Poddar**[1],†

[1]Department of Mechanical Engineering, Indian Institute of Technology Dhanbad (Indian School of Mines), Dhanbad, Jharkhand 826004, India

[2]Department of Mechanical Engineering, Meghnad Saha Institute of Technology, Kolkata, West Bengal 700150, India

(Received 20 February 2024; revised 19 July 2024; accepted 31 July 2024)

Understanding the effect of intricate surface wettability conditions on microswimmers is crucial for precisely navigating them across narrow microcirculatory networks. Here, we adopt the spherical squirmer model and Navier slip condition to delineate the microswimmer locomotion under a Poiseuille flow in a slit microchannel. Through a combined analytical–numerical approach utilizing bispherical coordinates and the superposition technique, we resolve the slip-modulated simultaneous hydrodynamic interaction with substrate boundaries. Phase portraits reveal that slip significantly alters propulsion mechanisms, destabilizing centreline stable oscillations of pullers beyond a threshold slip length. Superhydrophobic surfaces suppress near-wall rheotaxis states but preserve centreline focusing, facilitating slip-assisted directed transport without surface accumulation. Under strong background flows, subcritical Hopf bifurcation emerges for pullers at a critical slip length, transitioning dynamics from coexisting stable and unstable states to purely unstable behaviour. Contrastingly, for pushers, slip causes a transition from unstable to either stable or fixed-amplitude oscillations. Increased slip length reduces hydrodynamic repulsion on pullers from the walls by enhancing rotational velocity near the walls, whereas it counteracts the torque that causes unstable oscillations of pushers. Three-dimensional analysis of the trajectories reveals the significant role of the out-of-plane orientation of the microswimmer in its transitions between different swimming states. The presented regime maps offer parametric combinations for specific motion behaviours, guiding the development of smart microfluidic drug delivery systems and preventing biofilm deposition in biomedical devices.

Key words: micro-organism dynamics, active matter, microfluidics

† Email address for correspondence: antarip@iitism.ac.in

1. Introduction

Motile microorganisms often have to swim through confined geometries in their natural habitats, ranging from navigation of spermatozoa in the female oviduct (Elgeti, Winkler & Gompper 2015), movement of pathogens in lung mucus (Huffnagle, Dickson & Lukacs 2017) and deposition of infectious bacteria in the gastrointestinal tract, to phytoplankton in marine ecosystems (Barry *et al.* 2015). On the other hand, progress in microfluidic technology has led to the development of lab-on-a-chip devices to characterize in-flow microorganism dynamics to prevent urinary tract infection (Zhou *et al.* 2024) or improve clinically assisted reproduction (Huang *et al.* 2023). Furthermore, the artificial counterparts of microorganisms, termed micromotors and nanomotors, are being developed with an aim to achieve targeted drug delivery to infected sites by navigating through complex microcirculation networks (Baraban *et al.* 2013; de Ávila *et al.* 2017). Thus an understanding of their propulsive forces and interaction with restricted geometries is inevitable to ensure effective and precise manipulation within the confined pathways.

Interaction of microswimmers with physical boundaries significantly modifies their swimming attributes (Lauga *et al.* 2006; Berke *et al.* 2008; Di Leonardo *et al.* 2011; Molaei *et al.* 2014; Poddar, Bandopadhyay & Chakraborty 2021; Damor, Ghosh & Poddar 2023). The study of Berke *et al.* (2008) found that the bacterium *Escherichia coli* has a tendency to accumulate near the closest surface mainly due to the hydrodynamic forces that cause a wall-parallel reorientation to the swimming bodies. Hydrodynamic interactions with the boundary also lead to circular trajectories of swimming cells near a solid boundary, thereby explaining the mechanism of surface attachment responsible for biofouling and infection (Lauga *et al.* 2006). Similarly, the motility of sperm cells gets affected by the nearby boundary, as revealed in laboratory experiments (Cosson, Huitorel & Gagnon 2003). The surface entrapment of sperm cells poses a challenge to successful insemination in assisted reproductive technologies. Different micro- and nano-structured devices have been proposed (Guidobaldi *et al.* 2015; Nath *et al.* 2023) to prevent surface accumulation. Simultaneous theoretical models were developed to gain insight into the steady height and orientation of microswimmers near the wall during locomotion (Spagnolie & Lauga 2012; Ishimoto & Gaffney 2013; Li & Ardekani 2014), thereby validating the experimentally observed surface accumulation. Apart from hydrodynamic interaction with the surface, the motility of microorganisms is dependent on several other effects, such as direct flagellar contact (Kantsler *et al.* 2013), pairwise interaction (Drescher *et al.* 2011), thermal and intrinsic noise (Li & Tang 2009; Schaar, Zöttl & Stark 2015), complex rheology of the surrounding medium (Poddar, Bandopadhyay & Chakraborty 2019*a*), and short-range repulsive force (Walker *et al.* 2019).

The existing background flow modulates self-propulsion in quiescent environments, resulting in fascinating motion behaviours, e.g. navigating against the flow direction (Kaya & Koser 2012), cross-stream migration (Katuri *et al.* 2018), jumping or rolling (Sharan *et al.* 2022), and trapping in high-shear zones in a microchannel (Rusconi, Guasto & Stocker 2014). The change in orientation in response to velocity gradients gives rise to upstream navigation, widely known as 'rheotaxis' in relation to a variety of microswimmers, ranging from spermatozoa (Bretherton & Rothschild 1961; Kantsler *et al.* 2014) and bacteria (Hill *et al.* 2007) to artificial microswimmers (Palacci *et al.* 2015; Baker *et al.* 2019). Rheotaxis has different origins. For sperm in the neighbourhood of liquid–solid interfaces, it is governed by differential drag forces on the head and tail (Rothschild 1963). Combining microfluidic experiments and a mathematical model, Marcos *et al.* (2012) showed that rheotaxis can occur for *Bacillus subtilis* owing to a

critical interaction between the shape asymmetry of the flagella and the velocity gradients in the unbounded domain. Uspal *et al.* (2015) showed the possibility of rheotaxis near a single wall even in the absence of fore–aft asymmetry of the swimmer, e.g. spherical squirmers or Janus particles. The mechanism of shear-induced rotation constrains the upstream motion in the plane of shear. In subsequent investigations, the variations of similar rheotaxis phenomena were analysed for two-dimensional squirmers (Ishimoto 2017) and cylindrical-shaped micromotors (Brosseau *et al.* 2019), and in the presence of a repulsive wall interaction force (Walker *et al.* 2019). Similarly, modulations in the background flow can also take place due to an applied electric (Poddar *et al.* 2018, 2019*b*), thermal (Mantripragada & Poddar 2022; Poddar 2023), chemical or magnetic (Tottori & Nelson 2018) field.

The motion of microswimmers in confined vessels or channel-like environments brings a new dimension to the motion attributes compared to a single wall. The hydrodynamic interaction with the top and bottom walls leads to unique trajectories such as 'swinging' and 'tumbling' (Zöttl & Stark 2012). During their motion in channels, the existing pressure-driven flows in these passages compete with self-propulsion behaviour (Hill *et al.* 2007; Jana, Um & Jung 2012; Kaya & Koser 2012; Mathijssen, Pushkin & Yeomans 2015). In experiments, *Paramecium* describe helical trajectories in glass capillaries (Jana *et al.* 2012). Jana *et al.* (2012) also found that the travelling speed of the organism decreases with tighter confinements due to increased viscous resistance. Similarly, *Chlamydomonas sp.* cells migrate about the channel axis (Barry *et al.* 2015). Theoretical studies (Zöttl & Stark 2012; Zhu, Lauga & Brandt 2013) provided further insights by categorizing the swimming states for puller- and pusher-type microswimmers. They reported that puller microswimmers show stable locomotion at the channel centreline, while pushers end up crashing against the walls due to unstable swimming behaviour. It was also reported that swimmers with sufficiently strong dipole strength tend to reach stable states near the walls. In addition, the fluid inertia (Choudhary *et al.* 2022) and complex fluid rheology of microbiological flows (Mathijssen *et al.* 2016) strongly influence the swimming dynamics inside a channel. Recent experiments on microalgae *Chlamydomonas* (Omori *et al.* 2022) demonstrated the existence of rheotaxis and migration to the channel centreline in the presence of cyclic variations of the body deformation and swimming velocity. Along similar lines, oscillatory rheotaxis of self-propelling droplets in microchannels has been reported (Dey *et al.* 2022).

Surface properties of the geometric confinements have far-reaching consequences on microswimming behaviour. The experiments of Di Leonardo *et al.* (2011) and Lemelle *et al.* (2013) revealed that the circular swimming trajectories of *E. coli* bacteria change sense of rotation near a liquid–solid interface, categorized as an infinite or perfect slip interface. The numerical simulations of Pimponi *et al.* (2016) further predicted that no stable orbit exists for flagellated microswimmers near a similar interface. Surfaces with extreme wettability conditions have been created in various experimental scenarios, such as coating of hydrophobic molecules on surfaces handling a bacterial polymeric solution (Tretheway & Meinhart 2004; Lauga, Brenner & Stone 2005) or air bubble entrapment in micro- and nano-structured surfaces (Choi & Kim 2006; Lima & Mano 2015). The Navier slip model (Navier 1823) had been widely used to model such partial-slip boundaries in different contexts of microfluidics (Chakraborty 2008; Vega-Sánchez & Neto 2022). The superhydrophobic boundaries, having high slip lengths, reduce the interfacial friction and fundamentally alter the hydrodynamics. In natural microcirculatory networks, the Navier slip condition can mimic the role of the mucus layer that reduces the interfacial friction (Wang *et al.* 2020). The studies related to microswimmer dynamics near partial-slip

boundaries have been limited to either pure self-propulsion (Lopez & Lauga 2014; Hu *et al.* 2015; Poddar, Bandopadhyay & Chakraborty 2020) or linear shear flow near a wall (Ghosh & Poddar 2023). The mesoscopic simulations of Hu *et al.* (2015) suggested the potential of slip-patterned surfaces to convert circular bacterial motion to snaking trajectories. Moreover, contrary to free-slip interfaces, the partial-slip boundaries can produce stable swimming states only when the slip length crosses a critical strength (Poddar *et al.* 2020). Under a linear shear flow, the surface hydrophobicity creates a host of new rheotactic states (Ghosh & Poddar 2023) adjacent to the wall, indicating an enhancement in surface entrapment with wall slippage.

It is clear from the above discussion that no attention has been directed in the literature to answer how slip-induced alterations in the flow field around a microswimmer would interact with a background Poiseuille flow due to an applied pressure gradient in a microchannel. Poiseuille flow comes with the additional effects of a quadratic shear flow, which leads to a flow curvature due to the linearly increasing flow gradient. Depending on the unique self-propulsion mechanisms of front or rear actuation (for puller and pusher, respectively), a microswimmer may respond deferentially to the flow gradient in the presence of channel hydrophobicity, or it may need to overcome the drag induced by the flow. Again, the implications of two hydrodynamically interacting planar walls in a slit channel might give rise to non-trivial effects of slip length against the escaping trajectories observed in our earlier works (Poddar *et al.* 2020; Ghosh & Poddar 2023).

To address the above unresolved issues in the literature, we present a theoretical model of microswimmer locomotion under the simultaneous influences of Poiseuille flow and hydrodynamic slippage at the confining substrates. We obtain an exact solution of the Stokes flow for a sphere–wall geometry, and apply the superposition method to estimate the effects of both the confining boundaries simultaneously. We employ the Navier slip model (Navier 1823) to characterize the substrate wettability. In many earlier studies related to microswimmers in Poiseuille flow, researchers have focused on the force-dipole swimmer models (Mathijssen *et al.* 2016; Choudhary *et al.* 2022; Choudhary & Stark 2022), which illustrate the microswimmer as a point particle, thereby neglecting the effects of finite swimmer size (Spagnolie & Lauga 2012). To resolve this, we provide a semi-analytical solution to the mentioned problem in a bispherical coordinate system, which is competent in capturing the hydrodynamics of a spherical squirmer confined between parallel walls. Furthermore, the force dipole and an image system consisting of point force singularities can predict only the far-field dynamics. In contrast, the present methodology efficiently explains the near-field swimming attributes. Notably, a superposition of the background flow and the flow around a point-like microswimmer can provide important insights into the dynamics when the walls are no-slip in nature (Zöttl & Stark 2012). However, a mere inclusion of the Navier slip boundary condition in the background Poiseuille flow, without considering the hydrodynamic interaction with the channel walls, does not accurately represent the impact of slip length on the swimmer's dynamics. This is because the swimming velocity components that affect the dynamics remain unaltered with the slip effect in the absence of hydrodynamic interaction. The presently adopted spherical squirmer model accurately models the slip effects on the active swimming as well as the passive propulsion by incorporating the hydrodynamic interaction, thus rendering the outcome of the study far from intuitive. We further perform a detailed analysis of the dynamic system illustrating microswimmer motion, and categorize the different swimming behaviours.

Analysis of the dynamical system in the plane of background flow reveals the emergence of subcritical Hopf bifurcation with increasing slip lengths for puller microswimmers.

On the contrary, the unstable oscillations for pusher microswimmers either transition to damped oscillations or reach a fixed-amplitude oscillatory state. The interaction between a puller and a slippery surface is known to engender new surface rheotaxis states in linear shear flow (Ghosh & Poddar 2023). However, this impact does not create a new stable state at the channel centreline in Poiseuille flow; instead, it causes instability. In this case, it is the pushers that experience the emergence of new stable oscillatory states at the channel centreline due to the slip effect. Also, increasing slip length causes an enhanced tendency to swim downstream in a Poiseuille flow for the same pressure gradient of the imposed flow.

2. Problem formulation

Figure 1 illustrates the physical system under consideration. It displays a spherical microswimmer of radius a in a slit channel. The large width of a slit channel in the y direction lets us consider it as a confined passage between two parallel plates separated by a distance $\tilde{H}$ in the z direction. Here, the symbol $\tilde{}$ is used to denote dimensional quantities. The microswimmer is simultaneously actuated by its intrinsic swimming action and a background plane Poiseuille flow, which develops due to an imposed pressure gradient in the channel. The confining boundaries obey the Navier slip boundary condition, quantified by the slip length $\tilde{l}_s$. Here, the slip length ($\tilde{l}_s$) defines the imaginary distance below (bottom wall) and above (top wall) the bounding walls where the projected flow velocity vanishes. The mathematical form of the Poiseuille flow in the presence of wall slip takes the form

$$\tilde{\boldsymbol{u}}^{(ex)} = -\frac{1}{2\mu}\frac{\mathrm{d}\tilde{p}}{\mathrm{d}\tilde{x}}\left((\tilde{z}+\tilde{l}_s)\tilde{H}-\tilde{z}^2\right)\boldsymbol{e}_x, \tag{2.1}$$

where μ is the fluid viscosity, and $\mathrm{d}\tilde{p}/\mathrm{d}\tilde{x}$ is the applied pressure gradient in the longitudinal direction. The quadratic component in the Poiseuille flow (2.1) gives it a unique feature of non-vanishing shear stress gradient in comparison to a pure linear shear flow. In three dimensions, the orientation of the microswimmer is represented by the director vector $\hat{\boldsymbol{p}}$, whose orientation can be described by the angles θ_p and ϕ_p, as defined in figure 1. In puller microswimmers, e.g. bacterium *Chlamydomonas*, the forward movement is achieved by a pulling motion generated by the swimming apparatus located in the front part of the cell body, similar to a breaststroke action. For pusher microswimmers, e.g. sperm cells, the propulsion comes from a pushing motion generated by the posterior (rear) flagellar action. Without any background flow, the flow fields around the microswimmer are shown in the inset using red arrows, while the local forcing directions are marked with blue arrows.

We adopt the squirmer model (Lighthill 1952; Blake 1971) to describe the self-propelling mechanism of a spherical microswimmer. In this model, stimulation generated by the appendages of natural microswimmers is captured by small axisymmetric surface distortions on the sphere surface. These distortions are modelled by applying a tangential surface velocity ($\tilde{\boldsymbol{v}}_s^{(sp)}$) on the microswimmer surface:

$$\tilde{\boldsymbol{v}}_s^{(sp)} = \left(\frac{\hat{\boldsymbol{p}}\cdot\boldsymbol{r}_s}{|\boldsymbol{r}_s|}\frac{\boldsymbol{r}_s}{|\boldsymbol{r}_s|}-\hat{\boldsymbol{p}}\right)\sum_{n=1}^{\infty}\frac{2}{n(n+1)}B_n P_n'\left(\frac{\hat{\boldsymbol{p}}\cdot\boldsymbol{r}_s}{|\boldsymbol{r}_s|}\right), \tag{2.2}$$

where B_n is the amplitude of the nth squirming mode, P_n' refers to the derivative of the Legendre polynomial with respect to $\hat{\boldsymbol{p}}\cdot\boldsymbol{r}_s/|\boldsymbol{r}_s|$, and $\boldsymbol{r}_s$ denotes the position vector from the centre of the microswimmer to its surface. Following the previous literature

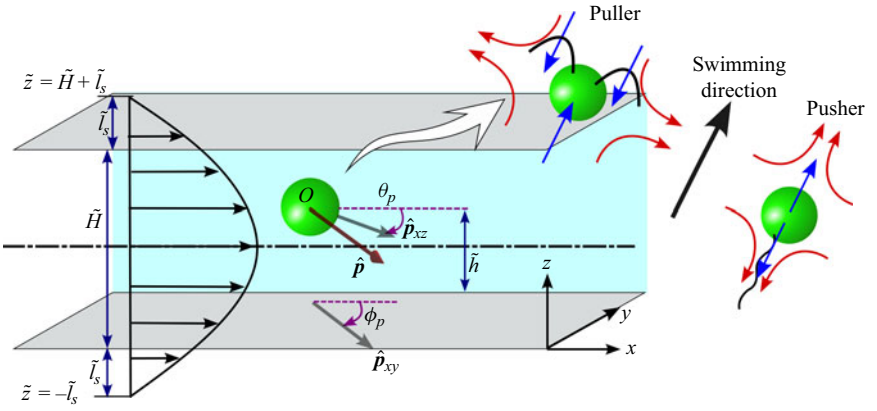

Figure 1. Schematics of a spherical microswimmer confined between two parallel slippery walls separated by distance $\tilde{H}$ in a background Poiseuille flow taking place in the x–z plane. The centre (O) of the sphere is located at height $\tilde{h}$ from the bottom wall, and the orientation vector is denoted $\hat{\boldsymbol{p}}$. The projection of $\hat{\boldsymbol{p}}$ on the plane of flow ($\hat{\boldsymbol{p}}_{xz}$) is inclined at an angle θ_p with respect to the x axis. Similarly, the projection of $\hat{\boldsymbol{p}}$ on the x–y plane, i.e. $\hat{\boldsymbol{p}}_{xy}$, makes an angle ϕ_p with the x axis. The inset portrays the swimming mechanisms of puller- and pusher-type microswimmers.

(Uspal *et al.* 2015; Shaik & Ardekani 2017), we truncate the infinite series in (2.2) up to the first two squirming modes to capture the essential physics of microswimming. The ratio between the second and first squirmer modes is defined as the squirmer parameter $\beta = B_2/B_1$, which categorizes the squirmers into pullers ($\beta > 0$), pushers ($\beta < 0$) and neutral microswimmers ($\beta = 0$).

In the following subsections, we develop a mathematical model to identify unique propulsive features due to the interaction between the microswimmer and the Poiseuille flow bounded by slippery confinements.

2.1. *Governing equations and boundary conditions*

For microorganisms having typical swimming velocity $\tilde{U}_{ref}$ ranging from tens to hundreds of μm s^{-1}, and characteristic length a up to a few hundred μm, the Reynolds number, defined as $Re = \rho \tilde{U}_{ref} a/\mu$, remains mostly of the order of 10^{-1} or even less (Lauga & Powers 2009). Thus we can neglect the inertial effects of the flow. It can also be shown that a similar size of microorganisms leads to a very small Péclet number, $Pe = \tilde{U}_{ref} a/D$, where D is the diffusion coefficient (Stark 2016). Accordingly, we neglect the Brownian dynamics (Ishikawa, Simmonds & Pedley 2006). In order to describe the locomotion of microswimmers in the creeping flow regime, we consider the Stokes equation (Lauga & Powers 2009). Further considerations of incompressible flow and a Newtonian fluid of viscosity μ reduce the governing equations to

$$\boldsymbol{\nabla} \cdot \tilde{\boldsymbol{v}} = 0 \quad \text{and} \quad -\boldsymbol{\nabla}\tilde{p} + \mu\, \nabla^2 \tilde{\boldsymbol{v}} = 0. \tag{2.3}$$

Considering the linearity property of the Stokes flow and boundary conditions, we can address the physics of self-propulsion due to squirming action (sp) and external Poiseuille flow (ex) as two separate Stokes flow contributions. Subsequently, the two effects are

combined using the relation

$$\gamma = \gamma^{(sp)} + \gamma^{(ex)}, \tag{2.4}$$

where γ represents velocity components attained by the microswimmer dictated by different flow triggering mechanisms, i.e. $\gamma \in \{\tilde{\boldsymbol{v}}, \tilde{\boldsymbol{V}}, \tilde{\boldsymbol{\Omega}}\}$.

We non-dimensionalize time by $a/\tilde{U}_{ref}$ and pressure by $\mu\tilde{U}_{ref}/a$. Here, we have considered the swimmer radius a as the length scale, and the velocity scale is set as $\tilde{U}_{ref} = 2B_1/3$ for non-dimensionalization. Finally, in a quiescent medium, the boundary condition on the microswimmer surface due to this squirming action becomes (Lee & Leal 1980)

$$\boldsymbol{v}^{(sp)} = \boldsymbol{V}^{(sp)} + \boldsymbol{\Omega}^{(sp)} \times \boldsymbol{r}_s + \boldsymbol{v}_s^{(sp)}, \tag{2.5}$$

where $\boldsymbol{V}$ and $\boldsymbol{\Omega}$ are the dimensionless translational and rotational velocities, respectively, and $\boldsymbol{v}_s^{(sp)}$ is the tangential squirming velocity.

The ambient flow can be considered to be a combination of linear (S) and quadratic (Q) shear components, defined as $\boldsymbol{v}_{S,\infty}^{(ex)} = \mathcal{V}_f(z + l_s)\boldsymbol{e}_x$ and $\boldsymbol{v}_{Q,\infty}^{(ex)} = \mathcal{V}_q z^2 \boldsymbol{e}_x$, respectively. Here, $\mathcal{V}_f = \tilde{u}_c/\tilde{U}_{ref}$ and $\mathcal{V}_q = -\mathcal{V}_f/H$ are the dimensional coefficients for linear and quadratic components, respectively, and $\tilde{u}_c = -(\tilde{H}^2/8\mu)(\mathrm{d}\tilde{p}/\mathrm{d}\tilde{x})$ denotes the centreline velocity in the plane Poiseuille flow in the absence of wall slip. This is the maximum velocity in the Poiseuille flow, and thus serves as a convenient scale for the external flow profile. Due to the presence of this external flow field, the sphere exhibits rigid body motion having its translational ($\boldsymbol{V}^{(ex)}$) and rotational ($\boldsymbol{\Omega}^{(ex)}$) velocity components. The existence of the sphere within the flow domain engenders a perturbation velocity field ($\boldsymbol{v}^{(ex)}$). Finally, the no-slip condition on the particle surface yields the following boundary condition for the perturbation velocity field ($\boldsymbol{v}^{(ex)}$):

$$\boldsymbol{v}^{(ex)} = \boldsymbol{V}^{(ex)} + \boldsymbol{\Omega}^{(ex)} \times \boldsymbol{r}_s - \boldsymbol{v}_\infty^{(ex)}. \tag{2.6}$$

The Navier slip boundary condition (Navier 1823) at the confinement boundaries relates the tangential components of the surface velocity at the confinement boundaries ($\tilde{\boldsymbol{v}}_\parallel$) to the local shear rate by the relation

$$\text{at } z = 0, H, \quad \boldsymbol{v}_\parallel = l_s \boldsymbol{n}_w \cdot (\boldsymbol{\nabla v} + (\boldsymbol{\nabla v})^{\mathrm{T}})(\mathcal{I} - \boldsymbol{n}_w \boldsymbol{n}_w), \tag{2.7}$$

where $\mathcal{I}$ is the identity tensor, and $\boldsymbol{n}_w$ represents the unit normal to the planar confinements towards the channel axis.

We consider the squirmer to be neutrally buoyant, and disregard any non-hydrodynamic forces that may arise due to surface interactions close to the walls. Hence we can compute the unknown microswimmer velocities $\boldsymbol{V}$ and $\boldsymbol{\Omega}$, generated due to the combined effect of squirming action and external Poiseuille flow, by employing the following force- and torque-free conditions:

$$\boldsymbol{F} = \iint_{S_p} \boldsymbol{\sigma} \cdot \boldsymbol{n_p}\, \mathrm{d}S = 0 \quad \text{and} \quad \boldsymbol{L} = \iint_{S_p} \boldsymbol{r}_s \times (\boldsymbol{\sigma} \cdot \boldsymbol{n_p})\, \mathrm{d}S = 0, \tag{2.8a,b}$$

respectively. The microswimmer attains the thrust force and torque required for its propulsion from both the squirming action ($\boldsymbol{F}_T^{(sp)}, \boldsymbol{L}_T^{(sp)}$) and the Poiseuille flow ($\boldsymbol{F}_T^{(ex)}, \boldsymbol{L}_T^{(ex)}$). These forces and torques are balanced by the hydrodynamic drag force ($\boldsymbol{F}_D$) and torque ($\boldsymbol{L}_D$) experienced by the microswimmer.

2.2. *Solution methodology*

We employ a combined analytical–numerical solution strategy for the Stokes flow (2.3) in a single-wall–squirmer configuration. The method is premised on the general solution of the Stokes equation using the eigenfunction expansion in the bispherical coordinate system (ξ, η, ϕ) (Lee & Leal 1980; Behera, Poddar & Chakraborty 2023; Poddar 2023). Our previous works contain a detailed description of the solution methodology for a single-wall system in the cases where a squirmer is in a linear shear flow (Ghosh & Poddar 2023) and in a quiescent medium (Poddar *et al.* 2020). The part of the boundary condition on the particle surface (2.6) that exists for a fixed particle in the ambient flow, i.e. $\boldsymbol{v}^{(ex)}(\text{at } r = 1) = -\boldsymbol{v}_{\infty}^{(ex)}$, is expressed in terms of the coefficients X_n^m, Y_n^m and Z_n^m (Lee & Leal 1980) to obtain the solution of the corresponding Stokes problem in terms of bispherical eigenfunctions. These constants, derived here for the case of a parabolic shear flow, are given as

$$X_n^1 = 0, \quad Z_n^1 = 0 \tag{2.9a,b}$$

and

$$Y_n^1 = -4\sqrt{2}\sinh(\xi_0)\,(n+\tfrac{1}{2})\,\mathrm{e}^{-(n+1/2)\xi}[\mathcal{V}_f + \mathcal{V}_q(\sinh(\xi_0)\,(n+\tfrac{1}{2}) + \cosh(\xi_0))], \tag{2.9c}$$

where ξ_0 corresponds to the location of the sphere surface in bispherical coordinates. The corresponding thrust force and torque components on the particle are given by

$$\begin{aligned} F_{(T,x)}^{(ex)} &= -\sqrt{2}\,\pi((l_s + \cosh(\xi_0)\,\mathcal{V}_f + \mathcal{V}_q(\cosh(\xi_0))^2)\sinh(\xi_0) \\ &\quad \times \sum_{n=0}^{\infty}[G_n^1 - H_n^1 + n(n+1)(A_n^1 - B_n^1)], \end{aligned} \tag{2.10a}$$

$$\begin{aligned} L_{(T,y)}^{(ex)} &= \sqrt{2}\,\pi(2\mathcal{V}_f + \mathcal{V}_q\cosh(\xi_0))\sinh^2(\xi_0) \\ &\quad \times \sum_{n=0}^{\infty}[\coth(\xi_0)\,\{n(n+1)(A_n^1 - B_n^1) + (G_n^1 - H_n^1)\} \\ &\quad - 2n(n+1)C_n^1 - (2n+1)(G_n^1 - H_n^1)]. \end{aligned} \tag{2.10b}$$

2.2.1. *Simultaneous influence of the two boundaries*

The bispherical method cannot be applied directly to calculate the hydrodynamic resistance offered by the two interacting parallel walls. To resolve this issue, we adopt the superposition method proposed in the literature (Ho & Leal 1974; Pasol *et al.* 2011; Ghalya *et al.* 2020). It was reported that the superposition of particle velocities obtained from the individual effects of the two walls could precisely capture the particle velocity in the presence of an external flow. The detailed numerical investigations (Jones 2004; Pasol *et al.* 2011) brought out that the superposition method is reasonably accurate in the range $H > 4$, i.e. when the channel width is broad relative to the particle radius. Along similar lines, in Appendix A, we compare our superposition method results against the detailed boundary-integral results of Staben, Zinchenko & Davis (2003) for the movement of a passive spherical particle placed between two infinite parallel walls in a plane Poiseuille flow. Good agreement between present calculations and the earlier results can be observed in figure 18. On the other hand, a similar superposition approach for two walls has also been used for the force dipole model of microswimmers (Zöttl & Stark 2012; Choudhary & Stark 2022). In the present method, the effective translational and rotational velocities

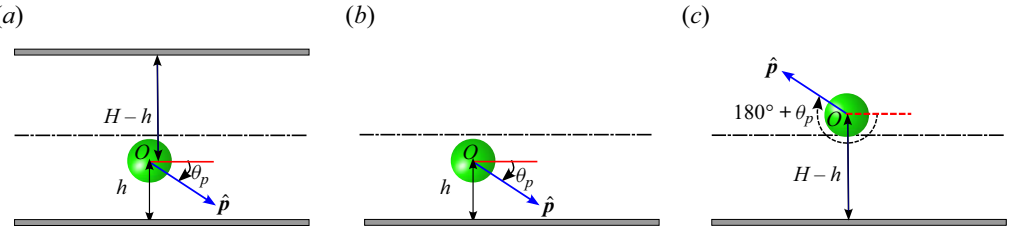

Figure 2. Schematics of the microswimmer configuration: (*a*) in the actual two-wall scenario; (*b*) relative to the lower wall only; and (*c*) relative to an equivalent lower wall for the upper wall.

are calculated by superposing the individual wall effects and subtracting the velocities in the unbounded domain to compensate for the repeated account of the same effect. Thus the velocity components can be obtained as

$$\boldsymbol{V} = \boldsymbol{V}^{(1)} + \boldsymbol{V}^{(2)} - \boldsymbol{V}^{(0)} \quad \text{and} \quad \boldsymbol{\Omega} = \boldsymbol{\Omega}^{(1)} - \boldsymbol{\Omega}^{(2)} - \boldsymbol{\Omega}^{(0)}, \tag{2.11a,b}$$

where $\boldsymbol{V}^{(1)}$ ($\boldsymbol{\Omega}^{(1)}$) and $\boldsymbol{V}^{(2)}$ ($\boldsymbol{\Omega}^{(2)}$) are the translational (rotational) velocities of the microswimmer due to the sole presence of the bottom and top wall, respectively. In addition, $\boldsymbol{V}^{(0)}$ and $\boldsymbol{\Omega}^{(0)}$ are the translation and rotation velocities of the microswimmer in Poiseuille flow in the absence of the bounding walls. Even though this approach remains intuitive for a passive particle, the asymmetry of a squirming sphere prohibits results from a single-wall scenario from being extrapolated to a corresponding two-wall situation owing to the different orientations of the director ($\hat{\boldsymbol{p}}$) relative to each wall, which is portrayed in figure 2. In figure 2(*c*), we show how the actual upper-wall–sphere configuration can be replaced by a conceptually equivalent lower-wall–sphere configuration. In the case of a passive particle, it would have been sufficient to consider the complementary distance $H - h$ from the top wall. However, in the case of microswimmer, one has to additionally account for the changed orientation of the director relative to the upper wall, i.e. $180^\circ + \theta_p$ instead of θ_p if the effect of the upper wall has to be calculated just by considering a single wall. Consequently, the velocity components $\boldsymbol{V}^{(2)}$ and $\boldsymbol{\Omega}^{(2)}$ of the upper wall have been calculated for the equivalent lower wall instead of the upper wall, as shown in figure 2(*c*). This orientational asymmetry about the centreline creates asymmetry in the microswimmer velocity components about the centreline, as shown in figure 3.

The velocity components of the microswimmer due to the self-propulsion in an unbounded domain are given by

$$V_x^{(sp,0)} = \cos(\theta_p), \quad \Omega_y^{(sp,0)} = 0 \quad \text{and} \quad V_z^{(sp,0)} = -\sin(\theta_p). \tag{2.12a–c}$$

The velocity components of a passive particle in a general ambient flow field $\boldsymbol{v}_\infty^{(ex)}$ in an unbounded domain can be calculated by invoking the Faxén law (Kim & Karrila 2013):

$$\boldsymbol{V}^{(ex,0)} = \left(\boldsymbol{v}_\infty^{(ex)} + \frac{\nabla^2 \boldsymbol{v}_\infty^{(ex)}}{6}\right)_{\text{at } z=h} \quad \text{and} \quad \boldsymbol{\Omega}^{(ex,0)} = \frac{1}{2}\,(\boldsymbol{\nabla} \times \boldsymbol{v}_\infty^{(ex)})_{at\ z=h}. \tag{2.13a,b}$$

Using the present form of external flow (2.1), we get

$$\boldsymbol{V}^{(ex,0)} = (\mathcal{V}_f(l_s + h) + \mathcal{V}_q(h^2 + \tfrac{1}{3}))\boldsymbol{e}_x \quad \text{and} \quad \boldsymbol{\Omega}^{(ex,0)} = \tfrac{1}{2}(\mathcal{V}_f + 2\mathcal{V}_q h)\boldsymbol{e}_y. \tag{2.14a,b}$$

The term $\mathcal{V}_q/3$ in the expression for $\boldsymbol{V}^{(ex,0)}$ signifies the effect of flow curvature on the particle motion in the unbounded domain.

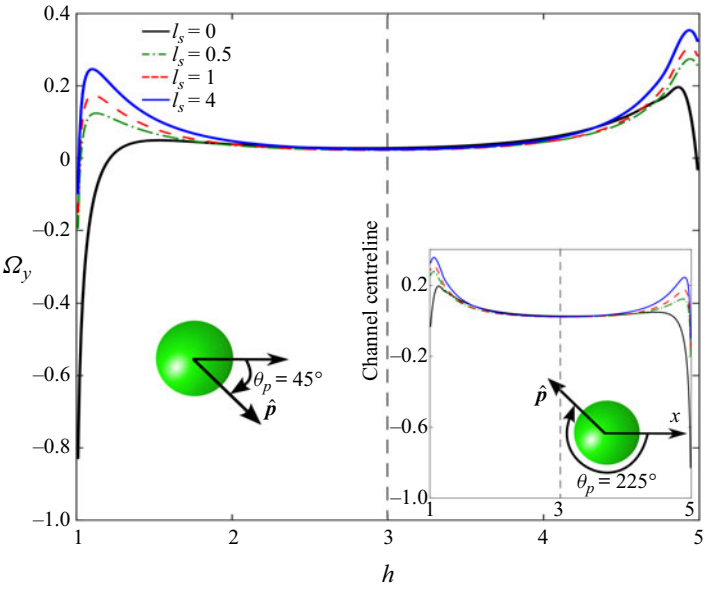

Figure 3. Variation of Ω_y of a puller microswimmer ($\beta = 3$) for varying gaps from the lower wall (h) and different slip lengths (l_s) in the absence of any external flow. The angular orientation is fixed at $\theta_p = 45°$ when measured relative to the lower wall. The inset shows the case $\theta_p = 225°$.

The mathematical model presented above brings out the following key dimensionless parameters influencing the flow physics: the slip length l_s, squirmer parameter β, channel height relative to the microswimmer radius H, and external flow strength relative to the intrinsic swimming speed $\mathcal{V}_f$.

2.3. *Three-dimensional dynamics*

The microswimmer axis may deviate from the x–z plane due to perturbations in actual experiments. Thus we perform a three-dimensional (3-D) analysis of the microswimmer dynamics to check the validity of the attractor fixed points and attractive limit cycles discovered in the above subsections against perturbation of the microswimmer axis in the vorticity direction.

Without hydrodynamic interaction of the microswimmer with the bounding walls, the two-dimensional phase-space remains similar to the 3-D problem (Zöttl 2014). However, the inclusion of hydrodynamic interaction in the model non-trivially alters the stability behaviour of near-wall fixed points. As reported in Uspal *et al.* (2015), for an external linear shear flow, some of the near-wall stable attractors may become unstable in three dimensions. To understand whether the slip length has any effect on our results, we calculate the out-of-plane dynamics as follows. Different components of the director vector can be expressed in a general 3-D space as

$$p_x = \cos\theta_p \cos\phi_p, \quad p_y = \cos\theta_p \sin\phi_p \quad \text{and} \quad p_z = -\sin\theta_p. \tag{2.15a–c}$$

Thus the quasi-steady dynamics (3.1) can be obtained by solving the following coupled ordinary differential equations (ODEs):

$$\frac{\mathrm{d}x}{\mathrm{d}t} = \mathcal{V}_f V_x^{(ex)} + V_x^{(sp)} \cos(\phi_p), \quad \frac{\mathrm{d}y}{\mathrm{d}t} = V_x^{(sp)} \sin(\phi_p), \quad \frac{\mathrm{d}z}{\mathrm{d}t} = V_z^{(sp)}, \tag{2.16a–c}$$

$$\frac{\mathrm{d}p_x}{\mathrm{d}t} = \Omega_y p_z - \Omega_z p_y, \quad \frac{\mathrm{d}p_y}{\mathrm{d}t} = -\Omega_x p_z + \Omega_z p_x, \quad \frac{\mathrm{d}p_z}{\mathrm{d}t} = \Omega_x p_y - \Omega_y p_x, \qquad (2.16d\text{–}f)$$

where

$$\Omega_x = -\Omega_y^{(sp)} \sin(\phi_p), \quad \Omega_y = \mathcal{V}_f \Omega_y^{(ex)} + \Omega_y^{(sp)} \cos(\phi_p) \quad \text{and} \quad \Omega_z = 0. \qquad (2.16g\text{–}i)$$

3. Results and discussion

This section demonstrates the locomotion behaviour of a microswimmer navigating through a confined Poiseuille flow in the presence of slippery walls. The estimation of the dimensionless parameters is based on various practical considerations, as mentioned below. In the microfluidic experiments of Junot *et al.* (2019), the flow rate of the external pressure driven flow was varied in the range $Q = 1$–6 nl s^{-1}, giving the maximum external flow velocity as $\tilde{u}_c = 28$–168 μms^{-1}, whereas the intrinsic bacteria velocity was found to be $\tilde{U}_{ref} = 20$–30 μm s^{-1}. On the other hand, the experiments of Dey *et al.* (2022) reported an intrinsic swimming speed $\tilde{U}_{ref} \approx 30$ μm s^{-1} for self-propelling droplets. The external flow rate used by them was comparatively lower, i.e. $\tilde{Q} = 0.04$–0.094 nls^{-1}, resulting in a maximum external flow velocity $\tilde{u}_c = 11.55$–27.15 μm s^{-1}. These available studies suggest the practical range of the dimensionless parameter $\mathcal{V}_f$ as 0.385–8.4. In view of these reported ranges of $\mathcal{V}_f$ and the values used in earlier theoretical studies (Zöttl & Stark 2012; Choudhary & Stark 2022), we have used $\mathcal{V}_f$ in the range 0–25. Unless mentioned otherwise, the results have been demonstrated for $H = 6$. We take into account two constraints imposed by the flow physics and the mathematical model for determining the distance H between the parallel plates. First, a very narrow channel violating the limit $H > 4$ may not provide accurate numerical results due to the breakdown of the superposition method (§ 2.2.1). Second, for a broad channel height, it is sufficient to consider the linear part of the external flow only near a wall (Katuri *et al.* 2018), thus obscuring the new physics of flow curvature associated with the parabolic shear flow. Further, motivated by the experimental evidence of varied slip lengths for diverse nano-engineered surface properties, such as hydrophobicity (Choi & Kim 2006) and 'intrinsic slippage' (Gentili *et al.* 2014), the results are demonstrated for a wide range of dimensionless slip lengths, i.e. $l_s = 0$–10.

The quasi-steady dynamics of the microswimmer can be described by solving the coupled ODEs

$$\frac{\mathrm{d}\boldsymbol{r}(t)}{\mathrm{d}t} = \boldsymbol{V}(\boldsymbol{r}(t), \hat{\boldsymbol{p}}(t)) \quad \text{and} \quad \frac{\mathrm{d}\hat{\boldsymbol{p}}(t)}{\mathrm{d}t} = \boldsymbol{\Omega}(\boldsymbol{r}(t), \hat{\boldsymbol{p}}(t)) \times \hat{\boldsymbol{p}}(t), \qquad (3.1a,b)$$

where the initial conditions required to solve these ODEs in the plane of external flow are specified as $\boldsymbol{r}(t = 0) = (0, 0, h_0)$ and $\hat{\boldsymbol{p}}(t = 0) = (\cos(\theta_0), 0, -\sin(\theta_0))$, where h_0 and θ_0 denote the initial height of the microswimmer centre from the bottom wall and its orientation angle, respectively. We have calculated the microswimmer trajectories by integrating (3.1*a*,*b*) using the fourth-order Runge–Kutta scheme (Chapra 2010). Here, we consider only the impacts of deterministic hydrodynamic forces, and ignore the stochastic forces (Shum, Gaffney & Smith 2010; Spagnolie & Lauga 2012). In addition, to avoid the effect of non-hydrodynamic forces due to surface interactions, we limit the lateral range of the computational domain to $1.01 \leq h \leq H - 1.01$. The microswimmer dynamics in the plane of external flow (i.e. x–z plane) can be captured by solving the plane

autonomous system

$$\frac{\mathrm{d}z}{\mathrm{d}t} = V_z(z,t) \quad \text{and} \quad \frac{\mathrm{d}\theta_p}{\mathrm{d}t} = \Omega_y(z,t). \tag{3.2a,b}$$

We make use of the dynamic system theory to understand the microswimmer dynamics. Due to the non-existence of explicit analytical expressions for the eigenvalues of the linearized system at fixed points, we employ a graphical approach to identify the stability criterion and observe instances of bifurcation. To this end, we generate phase portraits for the planar dynamics for a broad range parameters l_s and $\mathcal{V}_f$ chosen at fine intervals. Given the invariance of the dynamic system along x, we distinguish the motion behaviours in the upstream or downstream directions by computing the long-term trajectories for the critical cases observed in the phase portraits. It is noteworthy that in the absence of slip, combining the background flow and the flow around a point-like microswimmer provides crucial information on the dynamics even without hydrodynamic interaction (Zöttl & Stark 2012). However, mere inclusion of the Navier slip boundary condition (2.7) in the background Poiseuille flow, without incorporating the hydrodynamic interaction with the channel walls, cannot track the effect of slip length on the swimmer dynamics. This is because the microswimmer velocity components V_z and Ω_y remain unchanged with l_s when no hydrodynamic interaction is considered in the model. The hydrodynamic interaction is influenced by the slip effect, as described in figure 3. The figure shows that adjacent to the confining substrates, the rotational velocity of the microswimmer Ω_y significantly increases or even changes its sign in comparison to the no-slip scenario. Moreover, the inset with $\theta_p = 225^\circ$ in figure 3 displays a mirror symmetry of Ω_y variation relative to the $\theta_p = 45^\circ$ case, confirming an expected symmetry for self-propulsion between parallel walls in the absence of any external flow.

3.1. *Transition of swimming states for pullers*

We analyse the diverse swimming features of the pullers by categorizing the results into two broad ranges of $\mathcal{V}_f$, i.e. weak background flow ($0 \leq \mathcal{V}_f \leq 1$) and strong background flow ($1 < \mathcal{V}_f \leq 25$).

3.1.1. *Weak background flow regime*

The phase portraits for in-plane dynamics and corresponding sample trajectories in this regime are presented in figure 4. To shed light on the diverse physical processes represented by the phase portraits, we illustrate the effects of self-propulsion ('sp') and external flow ('ex') on various velocity components in figure 5. Moreover, we present regime maps highlighting different swimming states in figure 6 to summarize the impacts of various combinations of the governing factors on microswimming. Finally, the out-of-plane stability of the microswimmer and its long-time dynamics in three dimensions are described in figures 7 and 8.

Phase portraits with a low strength of the squirmer parameter, i.e. $\beta = 3$, are shown in figures 4(*a–c*). There exists an attractive spiral at the core of the phase space when a puller is confined between no-slip walls in a plane Poiseuille flow (figure 4*a*). This indicates damped amplitude oscillations of the microswimmer about the channel centreline. Similar motion features have been termed 'swinging' in the literature (Zöttl & Stark 2012). The corresponding trajectory in figure 4(*g*) demonstrates that these stable oscillations occur upstream to the flow direction (blue trajectory). At a sufficiently enhanced slip length ($l_s = 1.35$), the attractive spiral shows a slower decay (figure 4*b*). In addition,

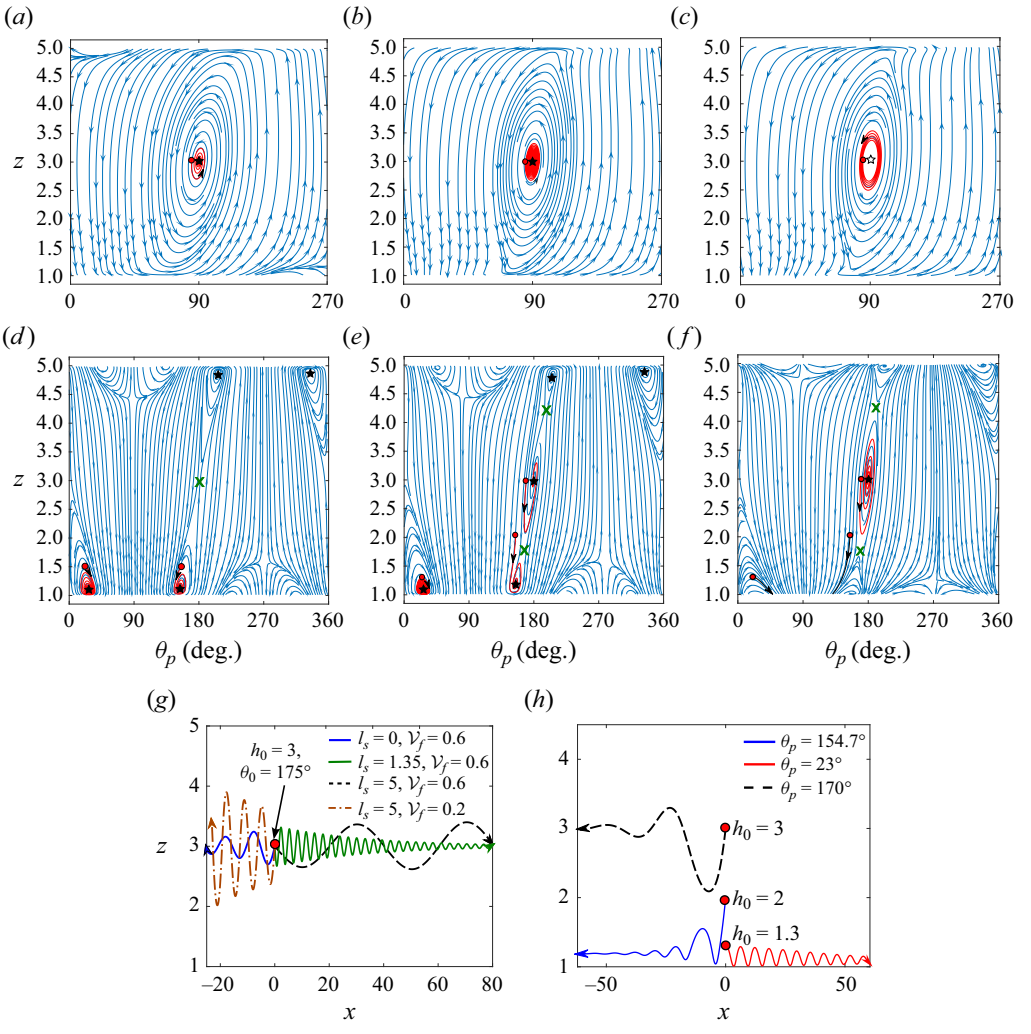

Figure 4. Phase portraits for in-plane dynamics and corresponding trajectories for a puller microswimmer. Different slip lengths in (*a–c*) are $l_s = 0$, 1.35 and 5, respectively, while other parameters are chosen as $\beta = 3$ and $\mathcal{V}_f = 0.6$. Squirmer parameter $\beta = 7$ is used in (*d*) $\mathcal{V}_f = 0.1$, $l_s = 0.05$, (*e*) $\mathcal{V}_f = 0.4$, $l_s = 0.05$, and (*f*) $\mathcal{V}_f = 0.4$, $l_s = 1.35$. The stable and unstable spiral states are indicated with filled and unfilled black stars, respectively, whereas the green crosses indicate the saddle points. The red lines in the phase portraits denote the corresponding selected trajectories in (*g*,*h*), with the red dots indicating the initial locations. (*g*) Different contrasting stable and unstable trajectories corresponding to the phase portraits in (*a–c*). (*h*) The contrasting feature of the coexistence of a near-wall stable and a centreline stable state corresponding to the phase portrait in (*e*). Trajectories at different combinations of l_s and $\mathcal{V}_f$ are presented for (*g*) $\beta = 3$ and (*h*) $\beta = 7$.

the axial motion switches to the downstream direction, as shown by the green curve in figure 4(*g*). This outcome carries substantial consequences in pressure-driven flow through a microchannel. They indicate the feasibility of reversing the motion direction of a microswimmer using the same pressure gradient in a slippery channel. This observation can be justified by the effects of hydrodynamic slip on the Poiseuille flow. Slip reduces the viscous friction offered to the flow by the walls. It can be shown that the effective flow rate is consequently increased by the factor $Q_{slip}/Q_{no\text{-}slip} = 1 + 6\,l_s/H$. As a result, the microswimmer experiences a greater force pushing it forwards in the direction of the flow,

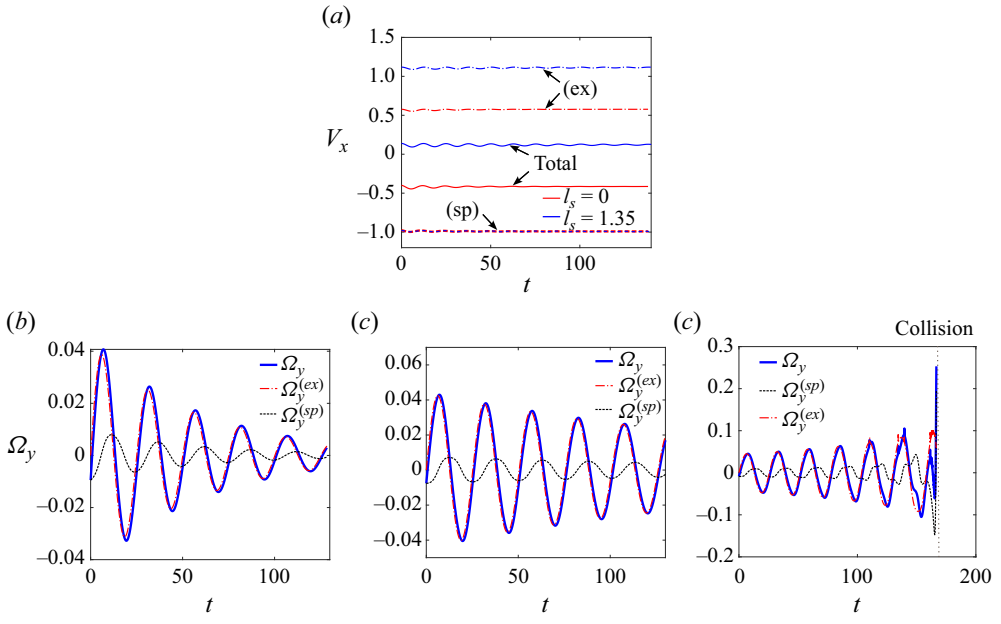

Figure 5. (*a*) Contributions of external flow strength and self-propulsion in V_x for different slip lengths. (*b–d*) Variations of Ω_y for $l_s = 0$, 1.35 and 5, respectively. Other parameters are $\mathcal{V}_f = 0.6$ and $\beta = 3$.

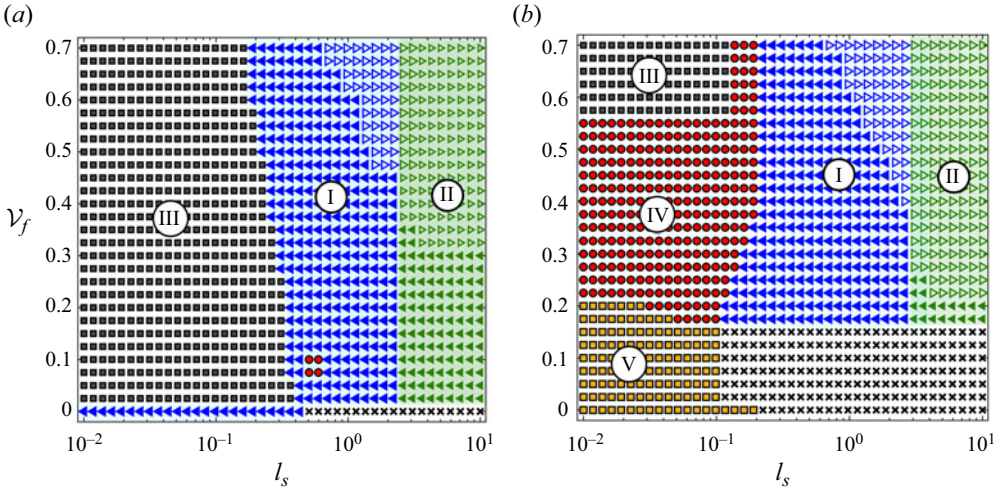

Figure 6. Regime maps for pullers with (*a*) $\beta = 3$ and (*b*) $\beta = 7$, for $\mathcal{V}_f < 1$. The different zones in the regime maps are designated as: (I) blue triangular markers for stable oscillation states about the channel centreline; (II) green triangular markers for unstable oscillation states about the channel centreline only; (III) black square markers for coexistence of near-wall (downstream) and centreline (upstream) steady states; (IV) red circular markers for coexistence of near-wall (upstream) and centreline (upstream) steady states; (V) yellow square markers for near-wall steady states (both upstream and downstream) only. In addition, the black cross markers denote the collision of the microswimmer with the walls. The downstream (upstream) oscillations are encoded in the triangular markers by pointing them towards the right (left).

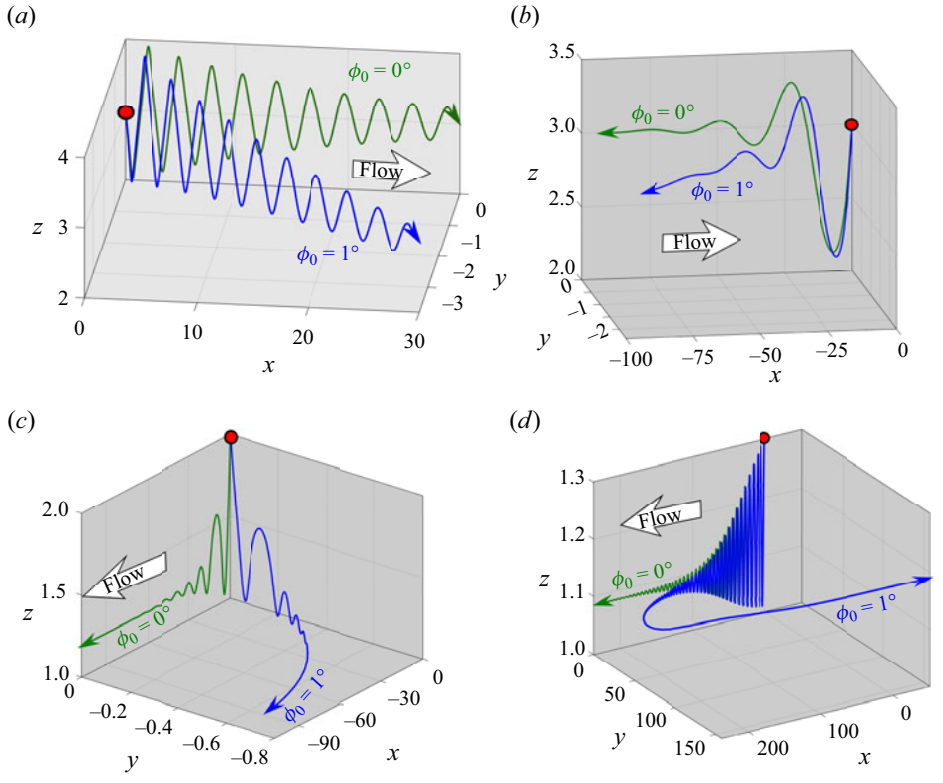

Figure 7. Comparison of trajectories of pullers for a small perturbation of the initial condition from the plane of external flow ($\phi_0 = 1°$) and those released in the plane of flow ($\phi_0 = 0°$). (*a*) Downstream centreline oscillations of a puller ($\beta = 3$) at $l_s = 1.35$ and $\mathcal{V}_f = 0.6$. (*b–d*) Highlighting the stability of (*b*) centreline and (*c*,*d*) near-wall trajectories of a puller ($\beta = 7$) with $l_s = 0.05$ and $\mathcal{V}_f = 0.4$. The centreline trajectories are captured at $h_0 = 3$ and $\theta_p = 165°$ in (*a*) and (*b*). Near-wall states are plotted for (*c*) $h_0 = 2$ and (*d*) $h_0 = 1.3$.

resulting in a greater tendency to swim in that direction. The effect of slip is not limited to the change in effective bulk flow rate. It has more significant consequences on the flow distribution, resulting in altered hydrodynamic interaction with the boundaries. This is reflected in the disruption of the stability condition at a high slip length, as observed in figure 4(*c*) for $l_s = 5$. The black curve in figure 4(*g*) shows that an unstable oscillation state is created in the downstream direction. Due to increasing amplitudes of oscillations, the swimmer finally crashes against one of the walls. It is to be noted that we have not included any repulsive interaction at the channel walls in order to focus exclusively on the hydrodynamic interaction behaviour (Zöttl & Stark 2012; Uspal *et al.* 2015). In figure 4(*g*), we have shown a case where an unstable upstream swimming state has been created at a lower strength of external flow ($\mathcal{V}_f = 0.2$) and high slip length ($l_s = 5$). Such differential motion behaviour indicates the competitive effects of slip length and flow strength on microswimmer locomotion.

The capacity of slip length to alter the swimming state along the centreline underlines the fact that slip effects on the dynamics are not restricted to the near-wall zones only, although the slip-induced perturbation for a fixed orientation of the swimmer vanishes at the centreline (figure 3). This apparent anomaly can be explained by the change in the near-wall velocities that alter the instantaneous configuration (h, θ_p) in such a manner that the swimmer still carries the signature of slip length when it moves far from the walls

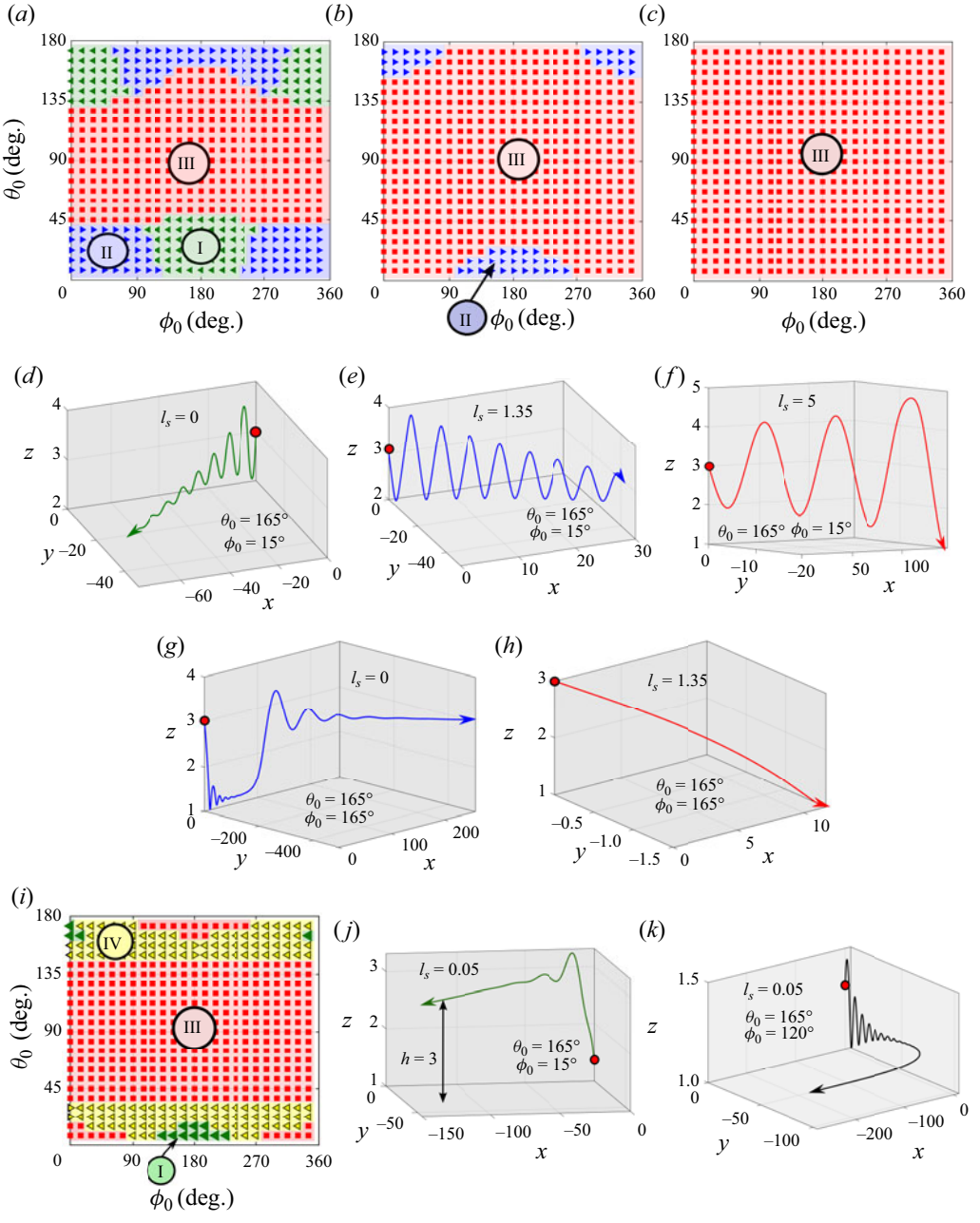

Figure 8. Out-of-plane dynamics of pullers in the weak background flow regime. (*a–c*) Regime maps for a puller ($\beta = 3$) summarizing the 3-D dynamics at different slip lengths $l_s = 0$, 1.35 and 5, and (*d–h*) corresponding trajectories. (*i*) Regime map to summarize the near-wall states for $\beta = 7$ and $h_0 = 1.3$, and (*j,k*) corresponding sample trajectories. Zones I (green), II (blue), III (red) and IV (yellow) represent centreline stable upstream, centreline stable downstream, collision, and stable near-wall state, respectively.

in subsequent time steps. Pullers experience repulsion from the confining walls during their oscillating motion due to wall-induced vorticity (Zöttl & Stark 2012). Hence the damped oscillations about the centreline are prominently observed for pullers in a plane Poiseuille flow with no-slip walls. However, slip length (l_s) reduces this repulsion by

enhancing the magnitude of the rotational velocity (Ω_y) near the confining walls (figure 3). Figures 5(*b–d*) illustrate the enhancement in the amplitude of Ω_y with time as the slip length is enhanced. In this scenario, the torque produced due to l_s alters the dynamics by suppressing the wall-induced vorticity. Simultaneously, the magnitude of the normal velocity (V_z) also gets enhanced abruptly, resulting in a collision state. Figure 5(*a*) shows that the slip length contribution to the translational velocity (V_x) is dominated by the external flow component. The flow-directed motion in the downstream direction gradually surpasses the upstream movement tendency due to intrinsic swimming.

Figure 6(*a*) provides a summary of different swimming zones that are attained by the microswimmer under varying levels of wall slippage (l_s) and flow strength ($\mathcal{V}_f$). The diverse dynamic traits can be categorized into five parametric zones: (I) blue triangular markers for stable oscillation states about the channel centreline; (II) green triangular markers for unstable oscillation states about the channel centreline; (III) black square markers for coexistence of near-wall (downstream) and centreline (upstream) steady states; (IV) red circular markers for coexistence of near-wall (upstream) and centreline (upstream) steady states; (V) yellow square markers for only near-wall steady states (both upstream and downstream). In addition, the black cross markers denote the collision of the microswimmer with the walls. The downstream (upstream) oscillations are encoded in the triangular markers by pointing them towards the right (left).

The phase portraits in figures 4(*d–f*) describe the dynamics for a high value of the squirmer parameter, i.e. $\beta = 7$. We observe near-wall stable states for $\beta = 7$. The regime map in figure 6(*b*) illustrates that a puller with a higher squirmer parameter ($\beta = 7$) exhibits near-wall steady motion (zone V), even in the presence of no-slip walls. A high value of the squirmer parameter signifies strengthened vorticity generation by the squirming action, thus providing the additional torque required to sustain stable oscillations in the wall proximity (see figure 4*d*). However, in the presence of a strong external flow, the mechanism of an enhanced flow vorticity due to the background flow sets in. For a stronger background flow ($\mathcal{V}_f > 0.2$), these competitive mechanisms of vorticity generation destroy the saddle point at the centre of the phase space, and convert it to a stable spiral and two pairs of near-wall stable spirals – saddle point doublets.

The near-wall stable fixed points located in the zone $90^\circ < \theta_p < 180^\circ$ were termed as 'rheotactic attractors' in the case of a pure linear shear flow adjacent to a single wall by Uspal *et al.* (2015) and Ghosh & Poddar (2023). These attractors signify an upstream swimming state at a fixed height and orientation (blue trajectory in figure 4*h*), indicating the tendency for boundary accumulation of microswimmers. Contrary to the findings in those studies, we observed near-wall rheotaxis at a much higher strength of the external flow, i.e. $\mathcal{V}_f \geq 0.225$. The additional hydrodynamic interaction with the upper wall in the presence of dual confinement, and the flow curvature associated with the quadratic shear component of the external flow, are responsible for this quantitative shift in behaviours. We further find that the near-wall attractors cease to exist for $\mathcal{V}_f > 0.55$ in the case of no-slip confinements (shown in figure 6*b*). The qualitative impact of the slippery wall on the stable states can be determined by studying the phase portraits in figures 4(*e,f*). For $\mathcal{V}_f$, an intermediate range of slip length $0.2 \leq l_s \leq 2$ causes destruction of the near-wall stable states, but sustains the centreline stable swimming. This opens up the scope of suppressing wall accumulation and achieving directed transport of microswimmers along the centreline of a microchannel. The competitive mechanisms are further influenced by the slip effects on both the intrinsic swimming and external flow. As a result, the near-wall stable states are converted to crashing states at elevated slip lengths.

We further identify the parametric regimes of coexisting stable states near the wall and at the channel centreline in zones III and IV in figures 6(*a*,*b*). Notably, the higher squirmer parameter case has prominence in these coexisting states.

In figure 7, we examine the out-of-plane stability of pullers corresponding to the phase portraits shown in figure 4(*b*) (for $\beta = 3$) and figure 4(*e*) (for $\beta = 7$). Figure 7(*a*) reveals that the centreline stable state in the downstream direction for $\beta = 3$ at $l_s = 1.35$ remains stable for a small out-of-plane perturbation ($\phi_0 = 1^\circ$). On the other hand, a puller with a stronger squirmer parameter, $\beta = 7$, displays a similar out-of-plane stability in the upstream direction (figure 7*b*). The attractor near the bottom wall (for $90^\circ \leq \theta_p \leq 180^\circ$) in figure 4(*e*) leaves the x–z plane for a small perturbation of $\phi_0 = 1^\circ$ but maintains its stable upstream swimming state, as shown in figure 7(*c*). In stark contrast, the in-plane near-wall attractor for $0^\circ \leq \theta_p \leq 90^\circ$ (figure 4*e*) loses its stability and the puller reorients from the downstream to upstream direction for a small out-of-plane perturbation (ϕ_0), as shown in figure 7(*d*). A similar phenomenon was reported previously for a squirmer in a linear shear flow over a no-slip planar wall (Uspal *et al.* 2015).

Taking cues from the instances of changed stability characteristics for small out-of-plane perturbations, we further provide an extensive 3-D analysis of the microswimmer dynamics based on long-time trajectory simulations for different governing parameters. The puller is considered to be released from an initial height $h_0 = 3$ for different initial orientations (θ_0, ϕ_0), and the motion characteristics are summarized in regime maps. The regime maps are plotted for ranges $7.5^\circ \leq \theta_0 \leq 172.5^\circ$ and $0^\circ \leq \phi_0 \leq 360^\circ$ with increments $\Delta\theta_0 = 7.5^\circ$ and $\Delta\phi_0 = 15^\circ$, whereas other parameters are similar to those in figures 4(*a*–*c*). The symmetry of the present problem about the channel axis allows us to limit the analysis for an in-plane angle to $\theta_0 = 180^\circ$ in the regime maps. At $\theta_0 = 0^\circ$ and 180°, the puller does not deviate from the channel axis during its motion due to the absence of any flow asymmetry.

Figure 8(*a*) describes that a puller ($\beta = 3$) exhibits stable oscillations towards downstream for $\theta_0 < 45^\circ$ at $\phi_0 = 0^\circ$. Further enhancement in θ_0 leads to a collision, followed by upstream stable states for $\theta_0 > 127.5^\circ$. Keeping θ_0 constant, if we increase ϕ_0, then the microswimmer can switch from a stable upstream to downstream direction, or the other way around. The stable upstream trajectory of a puller at $\theta_0 = 165^\circ$ and $\phi_0 = 0^\circ$ near a no-slip wall (blue curve in figure 4*g*) remains upstream at $\phi_0 = 15^\circ$ (figure 8*d*), but orients to downstream at an enhanced $\phi_0 = 165^\circ$ (blue curve in figure 8*g*). The downstream trajectory in figure 8(*g*) also remains stable about the centreline but displays some near-wall oscillations before the swimmer eventually reaches the channel axis. In the weak flow regime ($\mathcal{V}_f < 1$), the self-propulsion component remains competitive with the external flow. Hence the alternation in the direction of the navigation is due to the alternation of the self-propulsion component in (2.16*a*). At $\phi_0 = 90^\circ$, the cosine component of $\boldsymbol{V}_x^{(sp)}$ changes its sign, thereby making the resultant $\boldsymbol{V}_x$ positive. As a consequence, the microswimmer reorients towards downstream.

In agreement with the previous discussion corresponding to figure 4(*g*), the regime maps for 3-D analysis highlight the destruction of the upstream stable states (zone I in figure 8*a*) and their conversion to either downstream stable states or collision (figure 8*b*) at an enhanced slip length ($l_s = 1.35$). Nevertheless, a very high slip length ($l_s = 5$) results in a collision state regardless of the initial orientations (θ_0 and ϕ_0), as shown in figures 8(*c*,*f*). The out-of-plane angle (ϕ_0) also influences the $\boldsymbol{\Omega}_y^{(sp)}$ component, and the resultant $\boldsymbol{\Omega}_y$ (2.16*h*) remains insufficient to rotate the puller towards channel axis. Consequently, a

puller with a stable downstream trajectory shows a greater tendency to collide against the walls (figure 8*b*).

In order to capture the 3-D dynamics of the near-wall states observed at a higher squirmer parameter ($\beta = 7$), we plot another regime map in figure 8(*i*) for the parameters $l_s = 0.05$, $\mathcal{V}_f = 0.4$, and an initial launching height $h_0 = 1.3$. The regime map describes the existence of the downstream and upstream states near the bottom confinement for the ranges $15^\circ \leq \theta_0 \leq 35^\circ$ and $145^\circ \leq \theta_0 \leq 160^\circ$, respectively, at $\phi_0 = 0^\circ$. Beyond $\theta_0 = 160^\circ$, the puller exhibits large-amplitude oscillations about the channel axis and attains stability about the centreline. An increment of ϕ_0 changes the near-wall collisions to stable upstream motion, followed by centreline stable trajectories. Conversely, the stable centreline states beyond $\theta_0 = 160^\circ$ switch to near-wall stable states, followed by collision upon enhancement of ϕ_0. Comparing trajectories in figures 8(*j*,*k*) indicates a transition from a centreline stable state at $\phi_0 = 15^\circ$ to a near-wall stable state at $\phi_0 = 120^\circ$.

3.1.2. *Strong background flow regime*

For a strengthened background flow, the flow curvature effect becomes dominant, and the competition between the self-propulsion and Poiseuille flow takes a new turn, resulting in additional exciting features of the microswimmer dynamics. At flow strengths beyond a critical value $\mathcal{V}_f \geq 1.1$ (not shown), the stable and unstable oscillations about the channel axis coexist in accordance with the initial orientation of the squirmer, whereas the near-wall stable states vanish.

The enhanced strength of the Poiseuille flow ($\mathcal{V}_f \geq 5$) overpowers the axial velocity component due to squirming action, and the puller propels downstream irrespective of l_s. To represent the impact of slippery confinements, we provide a summary of swimming states in figure 9(*a*) for $\beta = 3$, and figure 9(*b*) for $\beta = 7$. These figures highlight a transition of dynamics due to enhanced slip length from simultaneous stable and unstable states (blue zone) to unstable states (red zone) only. The phase portrait in figure 9(*c*) provides insights into these swimming states. It shows that there exists a stable focus at the origin. The region of attraction is surrounded by an unstable limit cycle (green closed curve). The two trajectories shown in figure 9(*e*) illustrate the simultaneous existence of stable ($\theta_0 = 145^\circ$) and unstable ($\theta_0 = 120^\circ$) centreline oscillations at a very low value of slip length ($l_s = 0.01$).

For a high slip length $l_s = 3.6$, figure 9(*d*) shows the disappearance of the stable states. Figure 9(*f*) portrays an example of increasing-amplitude oscillations for a corresponding case. The regime maps (figures 9*a*,*b*) reveal that the disappearance of the stable states is observed at a critical value of slip length $l_s > 1.6$ for $\beta = 3$, and $l_s > 2.6$ for $\beta = 7$, when $\mathcal{V}_f = 5$. At the critical value of the parameter l_s, the unstable limit cycle shrinks down to the equilibrium point, and a sudden change from stable to unstable focus occurs. Thus we observe a subcritical Hopf bifurcation (Kuznetsov 1998). The varying boundaries between the blue and red zones in figures 9(*a*,*b*) demonstrate that the critical value of l_s for bifurcation reduces with either an enhancement in $\mathcal{V}_f$ or a weakened β. This observation emphasizes the significant interplay between the self-propulsion and external flow patterns facilitated by the substrate's wettability.

A puller experiences higher torque near the confinements due to a wall-induced flow vortex. Consequently, the director gains an enhanced rotational tendency away from the wall, and the puller crosses the channel centreline. However, the slip-mediated torque reduces the dominant external component of Ω_y, i.e. $\Omega_y^{(ex)}$, near the walls, as illustrated in figure 10. This observation is opposite to what happens in a weak flow regime where

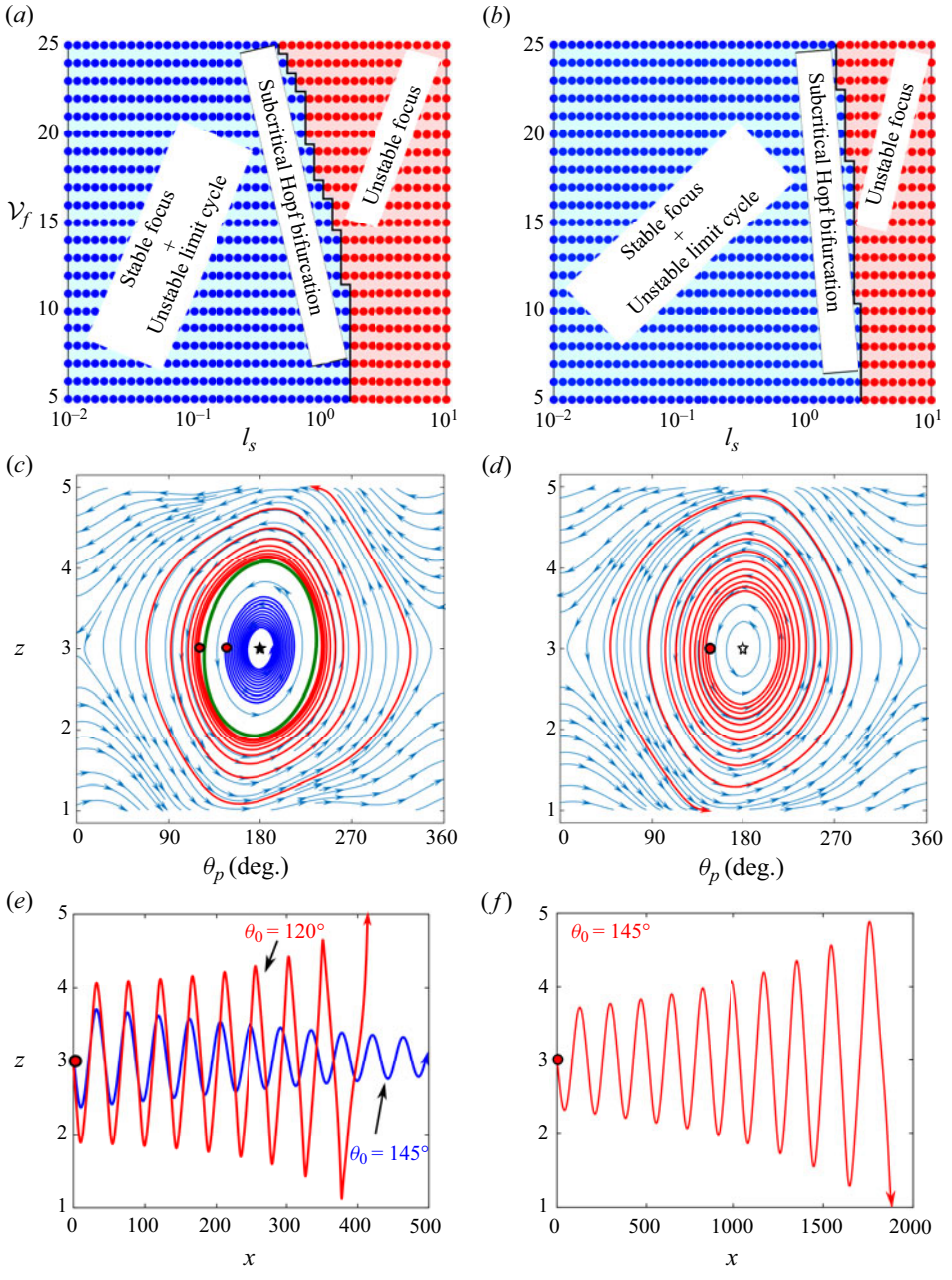

Figure 9. Regime maps for (*a*) $\beta = 3$ and (*b*) $\beta = 7$ in the strong background flow regime. Phase portraits (*c*) $l_s = 0.01$ and (*d*) $l_s = 3.6$ are for $\mathcal{V}_f = 7$. Trajectories are plotted for (*e*) $l_s = 0.01$, $\mathcal{V}_f = 7$), and (*f*) $l_s = 3.6$, $\mathcal{V}_f = 7$. All the phase portraits and trajectories are plotted for $\beta = 3$. Filled and unfilled stars show the fixed points corresponding to the stable and unstable spirals, respectively. The solid green curve in (*c*) shows the location of an unstable limit cycle, while the red dots indicate the launching state (h_0, θ_0).

the overall Ω_y is increased by slip (figure 3). Gradually, the external component of Ω_y is reduced to such an extent that the wall-induced dampening effect vanishes, only to result in unstable oscillations.

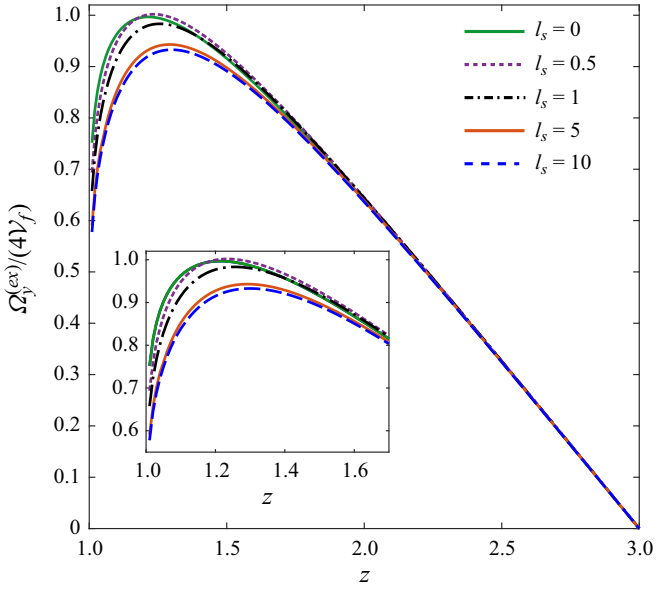

Figure 10. Rotational velocity contribution by the external flow $\Omega_y^{(ex)}/(4\mathcal{V}_f)$ for various slip lengths (l_s) and heights above the lower wall (z).

We summarize the out-of-plane swimming dynamics of pullers in the regime map of figure 11(*a*). Similar to the observations related to the in-plane dynamics, the strength of the flow overcomes the self-propulsion component and drives the puller downstream irrespective of the other parameters, β and l_s. Hence zone I is absent in this regime map. Figure 11(*b*) shows that at a smaller slip length ($l_s = 0.01$) and $\theta_0 = 165^\circ$, a puller exhibits damped oscillations when initially launched at $\phi_0 = 90^\circ$. However, it shows collision for an initial launching angle $\phi_0 = 165^\circ$, as shown in figure 11(*d*). On the other hand, for a smaller $\theta_0 = 45^\circ$, a comparison of figures 11(*c*,*e*) reveals a transition from unstable to stable oscillations, caused solely due to an increase in ϕ_0 from 90° to 172.5°.

3.1.3. *Alterations in focusing time*

The wall slip drastically modulates the strength of attracting spirals, indicating the influence on the time taken by the microswimmer to reach a steady state at the channel centreline. Following the work of Choudhary & Stark (2022), we quantify a focusing time parameter t_f as the time taken by the microswimmer to be trapped within $\pm 5\,\%$ of the channel half-height $H/2$. In agreement with §§ 3.1.1 and 3.1.2, the results reveal that the wall-induced dampening of the oscillations is opposed by increasing l_s, resulting in delayed focusing. Additionally, the puller exhibits both upstream and downstream focusing at $\mathcal{V}_f = 0.6$ (yellow markers) until the slip reaches its critical value for bifurcation. However, the puller focuses only in the downstream direction for a sufficiently strong external flow ($\mathcal{V}_f = 5$) (red markers in the inset of figure 12). Surprisingly, the swimmer takes a longer time to focus downstream with $\mathcal{V}_f = 5$ when compared to the $\mathcal{V}_f = 0.6$ case while keeping the slip length (l_s) constant. This phenomenon occurs because when the external flow ($\mathcal{V}_f$) is relatively weak, the intrinsic swimming can significantly contribute to the forward axial velocity V_x. However, in the presence of a strong external flow, the

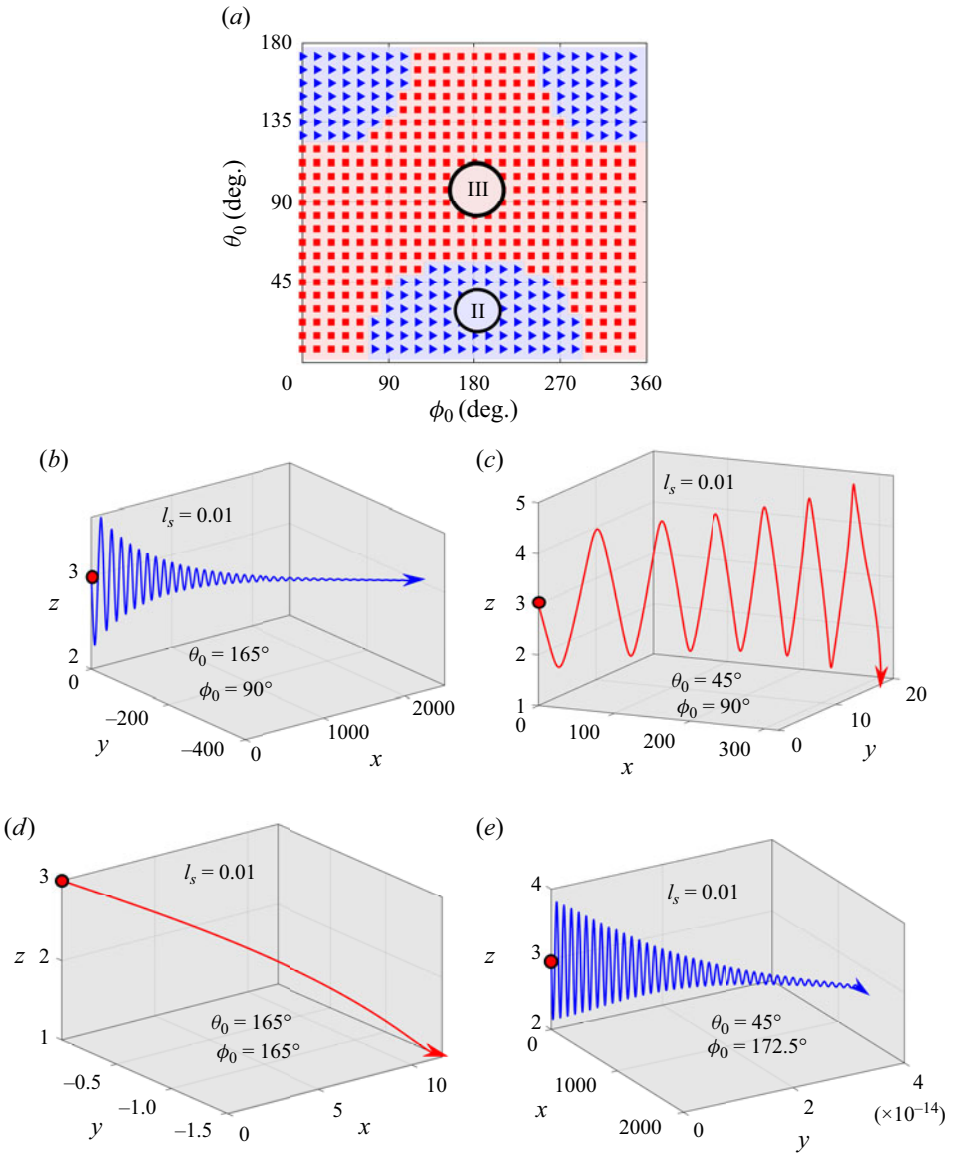

Figure 11. Out-of-plane dynamics of a puller ($\beta = 3$) in the strong background flow regime ($\mathcal{V}_f = 7$). (*a*) Regime map for $l_s = 0.01$, summarizing the out-of-plane dynamics for fixed initial height $h_0 = 3$. (*b–e*) Sample trajectory characteristics for different initial orientations θ_0 and ϕ_0.

self-propulsion has a much smaller effect on the overall V_x, and the axial motion is dictated mainly by the slip-affected background flow.

3.2. *Transition of swimming states for pushers*

In this subsection, we illustrate the interplay between slip length and relative flow strength on the locomotion strategy of a pusher. Figure 13(*a*) summarizes the trajectory attributes of a pusher ($\beta = -3$) for $0 \leq \mathcal{V}_f \leq 3.5$ and $0 \leq l_s \leq 10$. In a quiescent medium, the pusher collides (black cross markers) with the wall until a sufficiently large slip length

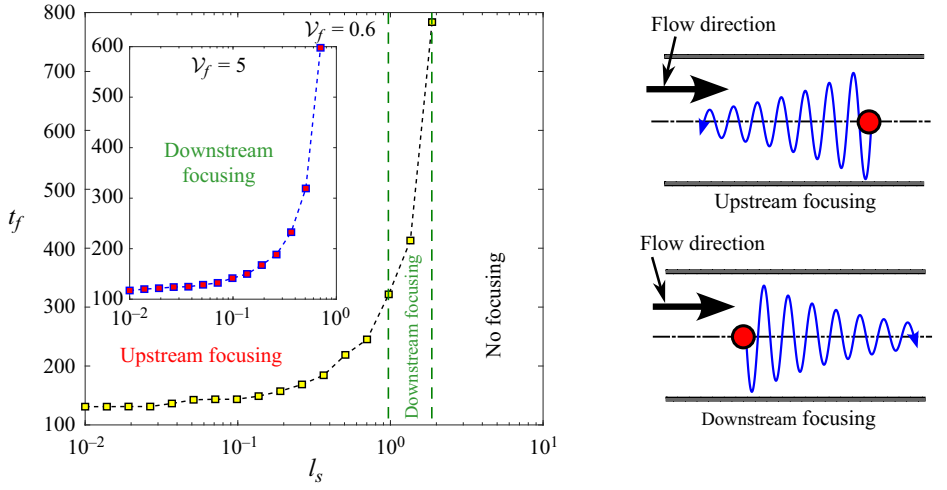

Figure 12. Variation of focusing time (t_f) of a puller ($\beta = 3$) with l_s at a fixed external flow strength $\mathcal{V}_f = 0.6$ and initial conditions $h_0 = 3$ and $\theta_0 = 160^\circ$; the results for $\mathcal{V}_f = 5$ are shown in the inset. The visual representations of upstream and downstream focusing are also shown.

stabilizes them near the wall (black square markers). In addition, the oscillations about the channel centreline are absent when there is no external flow. However, a minor enhancement in $\mathcal{V}_f$ alters these collision states to upstream unstable oscillations about the channel axis (blue filled triangles). We investigate the slip-affected dynamics in further detail by presenting phase portraits for $\mathcal{V}_f = 0.5$, $l_s = 0.02$ (figure 13*b*), $\mathcal{V}_f = 0.5$, $l_s = 5$, (figure 13*c*), $\mathcal{V}_f = 2$, $l_s = 0$ (figure 13*d*), and $\mathcal{V}_f = 2$, $l_s = 1.9$ (figure 13*e*), while their corresponding trajectories are presented in figures 13(*f*,*g*).

For a low range of slip length, the oscillations remain unstable, as reported in figures 13(*a*) (blue zone) and 13(*b*). The unstable spiral in the phase portrait in figure 13(*b*) indicates that only oscillations with increasing amplitude exist at $l_s = 0.02$ for $\mathcal{V}_f = 0.5$. Below a critical strength of external flow $\mathcal{V}_{cr} = 1.1$ (dashed red line in figure 13), a sufficiently strong slip length ($l_s > 4$) diminishes the amplitudes of these unstable oscillations, and an asymptotically stable spiral emerges at the core of the phase portrait, as presented in figures 13(*a*) (green square markers) and 13(*c*).

A comparison of phase portraits in figures 13(*d*,*e*) for the same high flow strength above the critical value ($\mathcal{V}_f = 2$) suggests the emergence of a stable limit cycle due to an enhanced slip length ($l_s = 1.9$). In figure 13(*e*), the stable limit cycle (black curve) surrounds the unstable spiral at the origin. Corresponding long-time trajectories in figure 13(*g*) illustrate that both stable (dashed red) and unstable (blue) oscillations saturate to a fixed amplitude, indicating the emergence of a limit cycle (black closed curve in figure 13*e*). Additionally, the limit cycle appears at lesser l_s, as portrayed in figure 13(*a*) with raising flow strength $\mathcal{V}_f$. Surprisingly, the birth of a stable limit cycle is not accompanied by a change of stability of the equilibrium point. It is important to note that the undamped oscillations appear even for non-slippery confinements, but only for a high flow strength $\mathcal{V}_f \geq 3.3$. This observation for no-slip walls being coherent (qualitatively) with the earlier observations of Zöttl & Stark (2012), the novelty of the present work is to uncover the transition of swimming states triggered exclusively by l_s for intermediate (1.1–3.3) and low (<1.1) values of $\mathcal{V}_f$. This result opens up the scope

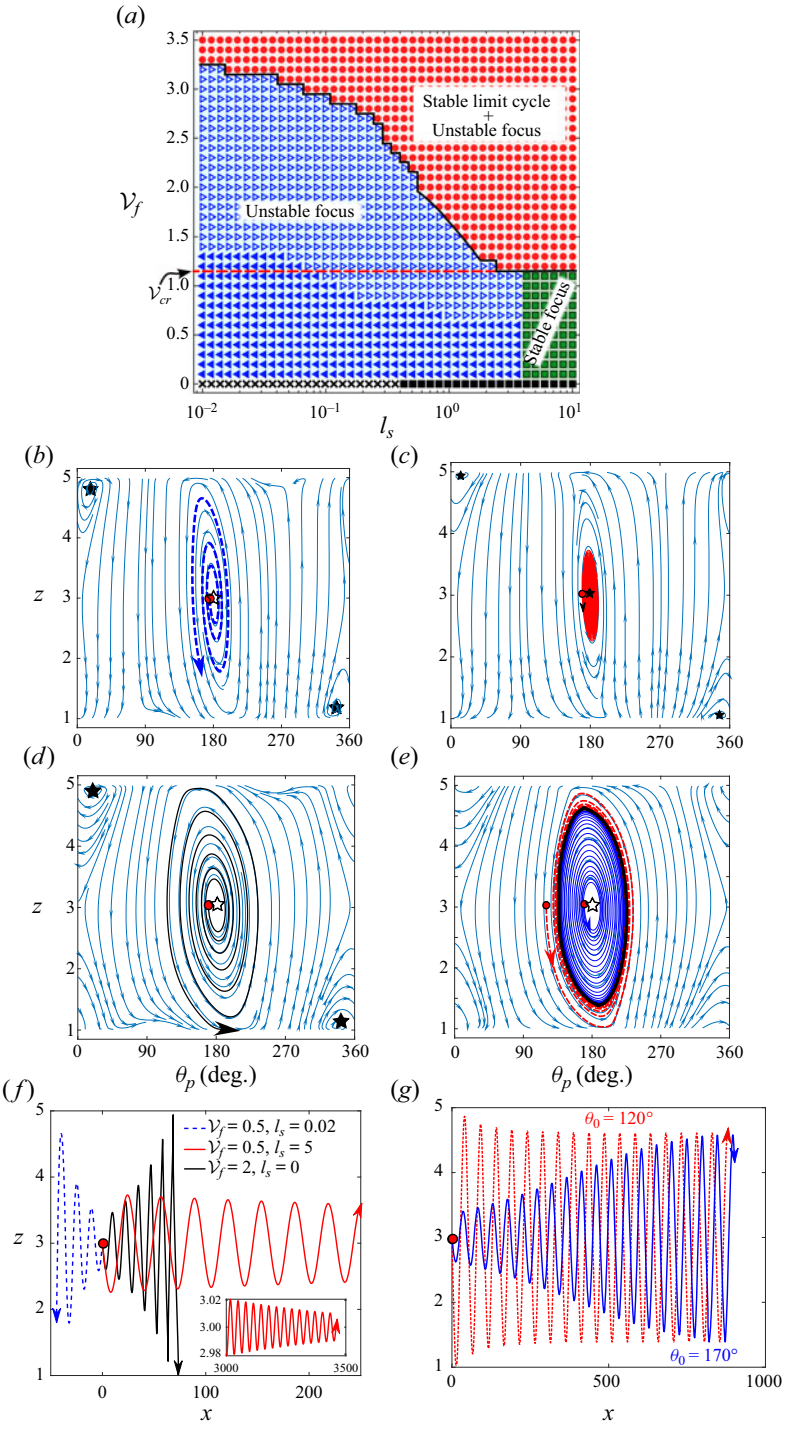

Figure 13. Motion attributes for a pusher ($\beta = -3$) for various $\mathcal{V}_f$ and l_s. (*a*) Regime map presenting a summary of the navigation of the pusher for different combinations of $\mathcal{V}_f$ and l_s. Different spiral states about the origin of phase space for (*b*) $\mathcal{V}_f = 0.5$, $l_s = 0.02$, (*c*) $\mathcal{V}_f = 0.5$, $l_s = 5$, (*d*) $\mathcal{V}_f = 2$, $l_s = 0$, and (*e*) $\mathcal{V}_f = 2$, $l_s = 1.9$. (*f*,*g*) The corresponding trajectories of the phase portraits in (*b*)–(*d*) and (*e*), respectively.

for centreline focusing of microswimmers even with a moderate strength of the pressure gradient of the external flow.

The unstable oscillations about the centreline between two no-slip walls can be attributed to the wall-induced torque (Zöttl & Stark 2012). The inclusion of slippery confinements provides the counter-torque to dampen those oscillations, and at a sufficiently large slip length, a pusher becomes asymptotically stable (figure 13*c*). We further analyse the modulations in Ω_y to gain insight into the underlying physics that leads to the formation of a stable limit cycle beyond $\mathcal{V}_{cr}$. The self-propulsion and background flow components of Ω_y increase in intensity with each oscillation (figure 14*c*). Nevertheless, the slip effect causes a decrease in the magnitudes of the Ω_y components (as shown in figure 14*d*). This result demonstrates the reduction in the thrust torque on the microswimmer near the walls with the augmentation in slip length. In this scenario, the slip-modulated flow vortex generates a greater torque in the anticlockwise (clockwise) direction near the bottom (top) wall, as compared to the cases where there is no slip. Consequently, the swimmer experiences the effective repulsion from both the walls required to attain a focused state. The effect of wall slip weakens when the launching orientations are close to the upstream configuration or the swimmer is far away from any of the walls. Consequently, as the slip-induced torque decreases, it eventually reaches a point where the oscillations can no longer be reduced, leading to a stable limit cycle (see figure 13*e*).

The out-of-plane stability of a pusher ($\beta = -3$) is examined in figure 15 for initial conditions $(h_0, \theta_0) = (3, 120^\circ)$. Other parameters ($\mathcal{V}_f = 2$, $l_s = 1.9$) correspond to those in figure 13(*e*), where the existence of a stable in-plane limit cycle has been reported. Comparison of the two curves in figure 15 indicates that the pusher remains stable for a small out-of-plane perturbation $\phi_0 = 1^\circ$.

To critically investigate the robustness of the above observation for any ϕ_0, we summarize the results of 3-D long-time simulations in figures 16(*a*,*b*), by choosing parameters similar to those in figures 13(*d*,*e*), respectively. It is evident from figure 16(*a*) that at a no-slip condition, pushers collide (denoted by red square markers) against the confinements irrespective of θ_0 and ϕ_0. This behaviour is further described by the trajectory in figure 16(*c*), which shows collision against the bottom wall under initial conditions $\theta_0 = 60^\circ$ and $\phi_0 = 180^\circ$. However, we can observe the existence of both stable (green circular markers) and unstable limit cycles (yellow circular markers) at an enhanced slip length, as shown in the regime map (figure 16*b*). At $\phi_0 = 0^\circ$, the stable (figure 16*d*) and unstable (figure 16*f*) limit cycles are found within the range $108^\circ < \theta_0 < 145^\circ$ and $145^\circ \leq \theta_0 \leq 179^\circ$, respectively. Limit cycles at $\phi_0 = 180^\circ$ are unstable (figure 16*e*) within the range $1^\circ < \theta_0 \leq 35^\circ$, and stable (figure 16*g*) within the range $35^\circ < \theta_0 \leq 72^\circ$. Further exploration reveals that these oscillating states for pushers are highly sensitive to ϕ_0. These stable and unstable oscillations exist near the x–z plane for a deviation of the azimuthal angle (ϕ_0) of $\pm 4^\circ$ from the plane. The existence of these stable and unstable oscillating states near $\phi_0 = 0^\circ$ or 180° is governed by the cosine component of $\Omega_y^{(sp)}$ in (2.16*h*), which becomes competitive with $\Omega_y^{(ex)}$. Hence the pusher orients towards the channel axis. Similar to the pullers, pushers also navigate along the channel axis at $\theta_0 = 0^\circ$ and 180° for all ϕ_0.

3.3. *Effect of channel height*

The degree of confinement is dictated by the distance between the two slippery walls (H). An increase in H signifies a decrement in the flow curvature, thus the quadratic component

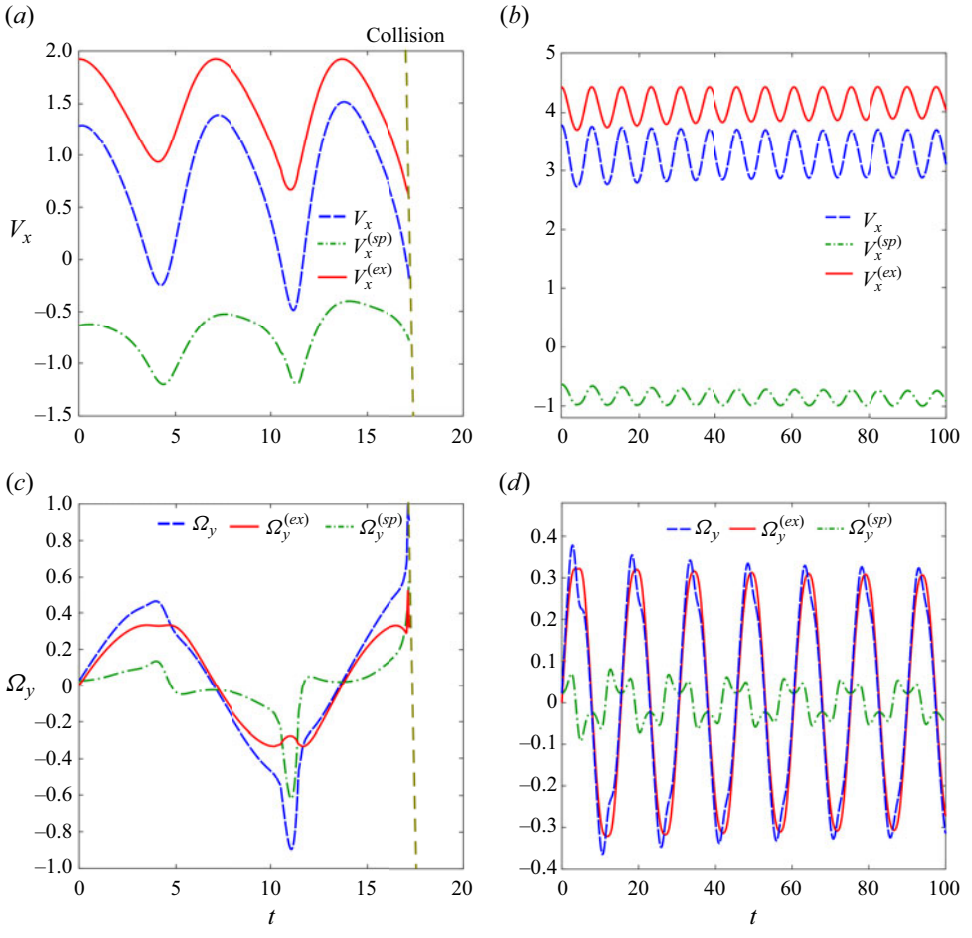

Figure 14. Plots of (*a*) V_x and (*c*) Ω_y displaying different velocity components of a pusher ($\beta = -3$) at $l_s = 0$. (*b*,*d*)) The effects of slip length $l_s = 1.9$on the velocity components for the similar squirmer parameter. Other parameters are $\mathcal{V}_f = 2$, $h_0 = 3$ and $\theta_0 = 120^\circ$.

of the background flow weakens. Again, the expression for the enhancement factor for the effective flow rate $Q_{slip}/Q_{no\text{-}slip} = 1 + 6\,l_s/H$ suggests that to retain the same slip-induced effect for walls at a further distance, a corresponding increment in slip length is also required. Qualitative changes in swimmer dynamics have evolved due to these quantitative changes in flow physics. For example, the unstable states are found for $H = 6$ and $H = 8$ in figures 4(*c*) and 17(*a*), respectively. However, the phase portrait in figure 17(*b*) for the same slip length but with a much higher channel height ($H = 14$) highlights a stable swimming state, suggesting that the critical slip length for the bifurcation has not yet been reached. Following such qualitative changes, it can be determined that the different regime boundaries shown in the regime maps of figures 6 and 9(*a*,*b*) would shift towards higher l_s if the channel walls are located at farther distances.

4. Conclusions and remarks

In summary, we have investigated theoretically how the hydrodynamic slip at the walls affects the movement of a microswimmer in a narrow channel under a background

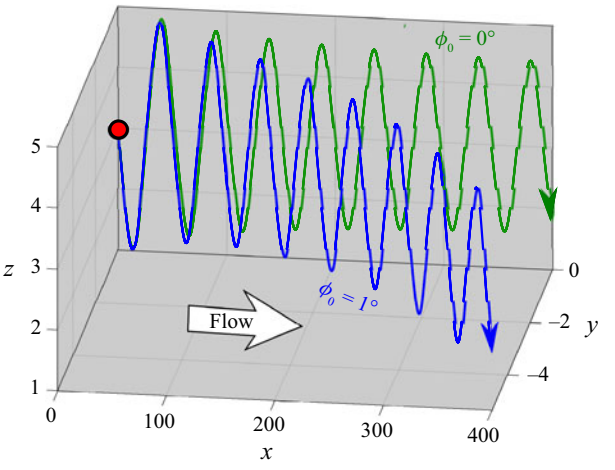

Figure 15. Comparison of the trajectory of a pusher ($\beta = -3$) at $l_s = 1.9$, $h_0 = 3$ and $\theta_0 = 120°$ for a small perturbation of the initial condition from the plane of external flow ($\phi_0 = 1°$) with that released in the plane of flow ($\phi_0 = 0°$).

pressure-driven flow. The microswimmer has been modelled as a spherical squirmer, which can be a puller or pusher based on the variation in the micro-propulsion mechanism. The hydrodynamics in the Stokes flow regime has been solved using a combined analytical–numerical technique in bispherical coordinates. The superposition method has been employed to capture the simultaneous hydrodynamic interaction with the top and bottom walls. The dynamical system comprising two coupled ordinary differential equations (3.4) provides deep insight into the microswimming. By combining the findings of phase space analyses of the dynamical system and computed long-time trajectories, we have uncovered a host of novel dynamic behaviours influenced by the key parameters – dimensionless slip length (l_s), squirmer parameter (β) and flow strength relative to the reference self-propulsion velocity ($\mathcal{V}_f$). We have further provided physical insights into the changes in swimming behaviour by examining the slip-induced modulations on various flow-governing mechanisms and their influence on the microswimmer's velocity components. A three-dimensional (3-D) analysis of the microswimmer dynamics has been performed to check the robustness of the in-plane attractor fixed points and attractive limit cycles against perturbation of the microswimmer axis in the vorticity direction.

Diverse motion behaviours of pullers emerge for low ($\mathcal{V}_f < 1$) and high ($\mathcal{V}_f > 1$) flow strengths. In the weak flow regime, the centreline stable swimming states are observed for no-slip walls when the microswimmers are launched anywhere in the channel, excluding the states that lead to crashing against walls. Augmenting slip length beyond a critical point brings in a qualitative change in the swimming behaviour, and the stable spiral at the phase space origin is converted to an unstable spiral, signifying increasing-amplitude oscillations. In addition, a high value of the squirmer parameter β gives rise to additional stable states in the wall proximity due to the greater strength of vorticity generation by the squirming action. An increase in slip length annihilates the near-wall steady states by shifting them further downwards. We further report the existence of different swimming states, triggered at different combinations of l_s and $\mathcal{V}_f$, in the phase maps of figure 6. Centreline focusing without wall accumulation results for high flow strengths beyond a critical value $\mathcal{V}_f \geq 1.1$. Depending on the initial launching orientation, the swimmer shows either stable or unstable oscillations about the channel axis (figure 9*c*). However, a

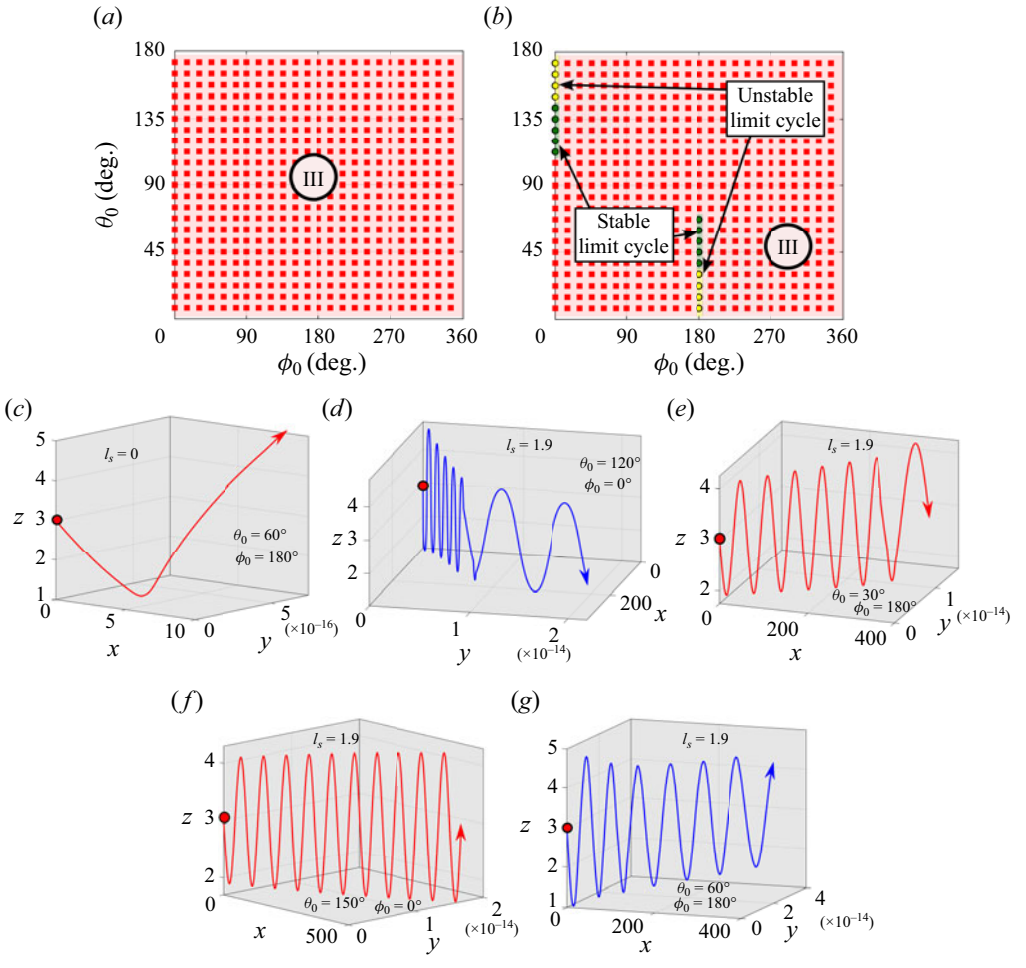

Figure 16. Out-of-plane dynamics of a pusher ($\beta = -3$) for $h_0 = 3$. The summary of the 3-D motility characteristics are in the regime maps for (*a*) $l_s = 0$, and (*b*) $l_s = 1.9$. (*c–g*) Different 3-D trajectories of a pusher for different initial orientations θ_0 and ϕ_0. In the regime maps, the stable and unstable limit cycles are highlighted with green and yellow markers, respectively.

high slip length destabilizes the motion. The transition of dynamics from coexisting stable and unstable states to pure unstable dynamics marks the existence of subcritical Hopf bifurcation with l_s as the bifurcation parameter. It has also been found that enhancing $\mathcal{V}_f$ or weakening β causes an early onset of bifurcation (figure 9), but only when the channel walls are significantly hydrophobic.

The wall slip has a dissimilar impact on the dynamics of a pusher. Here, the slippery transition occurs from only unstable to either only stable oscillations or fixed-amplitude oscillations about the channel axis (figure 13). It has also been observed that the state transition due to increasing slip occurs for lower values of $\mathcal{V}_f$ as compared to the no-slip case.

An observable trend of the slip effect is the shift from upstream swimming states to downstream states, both stable and unstable, under the same pressure gradient of the external flow. The hydrodynamic slip acts to reduce the viscous friction at the substrate

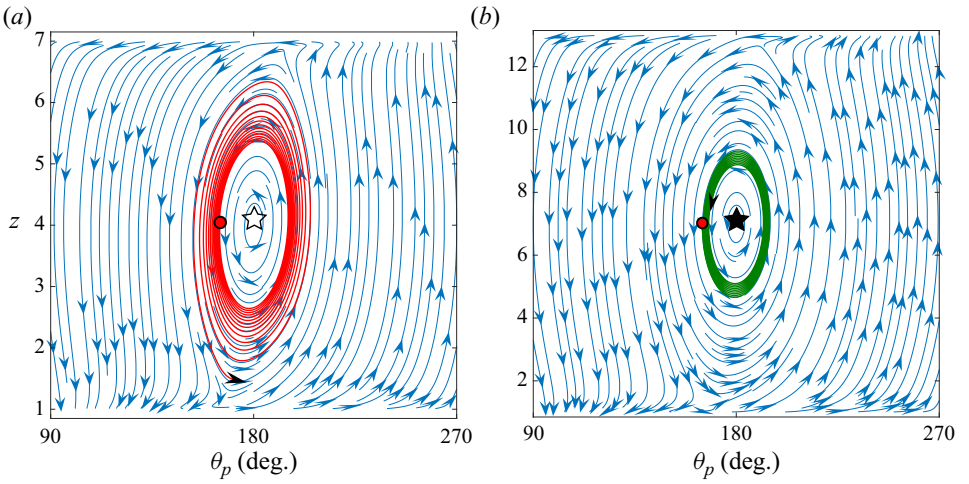

Figure 17. Phase portraits for pullers for varying channel heights: (*a*) $H = 8$ and (*b*) $H = 14$. Other parameters are $\mathcal{V}_f = 0.6$, $l_s = 5$ and $\beta = 3$. Filled and unfilled stars show the fixed points corresponding to the stable and unstable spirals, respectively. Also, red and green lines describe sample phase space trajectories to confirm the nature of spirals.

interface, leading to an increase in the effective flow rate by a factor $Q_{slip}/Q_{no\text{-}slip} = 1 + 6\,l_s/H$, which results in enhanced thrust in the forward direction.

The changes in the strength of attractive spirals at the phase space origin caused by slip indicate its impact on the focusing time, which is the time taken by the swimmer to be trapped at the channel centreline. However, the contest between the external and intrinsic components of the axial velocity (V_x) leads to the counter-intuitive result of longer focusing time with an increase in flow strength (figure 12). Moreover, increasing the channel height calls for an increased slip length to observe the same qualitative modulations in swimming states as reported in this study.

The outcomes of our study reveal the complex interaction between the motion induced by the background flow and the inherent swimming ability in the presence of hydrodynamic slippage. Moreover, the wall slip exerts opposing effects on the dynamics of the puller- and pusher-type microswimmers. In the case of pullers, the wall-induced vorticity induces effective repulsion from both the walls, and the oscillations about the centreline are dampened as a consequence. An increase in slip length (l_s) reduces this repulsive action by increasing the magnitude of the rotational velocity (Ω_y) near the confining walls (figure 3). As a consequence, instability appears in the microswimmer motion. On the other hand, unstable oscillations about the centreline between two no-slip walls occur in the case of pushers due to the contrasting mechanism of self-propulsion. Here, a hike in slip length supplies the counter-torque to dampen those oscillations, and as the slip length crosses a critical value, the pusher reaches an asymptotically stable state at the channel centreline.

The extensive 3-D analysis of the microswimmer trajectories brings out the significance of the out-of-plane angle (ϕ_0) on the transition between different states. The transition from a stable upstream to a stable downstream state, and from stable downstream to collision states, can be observed in the regime maps shown in figures 8(*a–c*) during the weak background flow regime of puller microswimmers. When the pullers experience a strong background flow, increasing the initial orientation (ϕ_0) can cause the motion to transition

from stable downstream movement to collision states, and *vice versa* (see figure 11*a*). The out-of-plane angle (ϕ_0) modulates the squirming component of $\boldsymbol{V}_x$ and $\boldsymbol{\Omega}_y$, which in turn alter the resultant translational and rotational velocity components to determine the motility characteristics. Contrastingly, for pushers, the stable and unstable limit cycles at high slip length sustain only up to a slight deviation of initial orientation ($\phi_0 \approx \pm 4^\circ$) from the plane of the external flow (figure 16*b*). In this scenario, the inadequate squirming component of $\boldsymbol{\Omega}_y$ cannot rotate the pusher towards the channel axis, and a direct collision results beyond the mentioned range of ϕ_0.

Thus the present study is a precursor in delineating the complicated flow physics associated with the hydrodynamic slip in microchannel carrying microswimmers under a pressure-driven flow. The theoretical insights presented could inspire novel experiments to harness the hydrophobicity of surfaces as a means of achieving desired transport properties for microswimmers, ranging from on-demand switching of motion direction for the same pumping power of the background flow, and better mixing of solutes in microchannels due to oscillatory microswimmer motion between different fluid layers, to suppressing wall accumulation and achieving focused transport along the channel centreline. Moreover, the regime maps in figures 6, 9 and 13 may turn out to be crucial in choosing an optimal set of parameters while designing smart actuation systems (Fischer 2018) for controlled guidance of microswimmers.

Future investigations focusing on the modulations of the reported results in scenarios where the channel height is comparable to the size of the microswimmer may complement our understanding of the physical problem discussed here. Moreover, the effect of the elongated shape of certain microorganisms (Shum *et al.* 2010; Kumar & Ardekani 2019) may interact with the shear-induced rotation, and create new stable states along the channel centreline in the presence of wall slip. However, a major challenge in extending the present analysis using the boundary element method (Staben *et al.* 2003; Zhu *et al.* 2013) or the multipole extension method (Pasol *et al.* 2011), adopted earlier for a similar configurations, is the Navier slip boundary condition at the substrate–fluid interface, which adds to the complexity of theoretical calculations. On the other hand, a possible difficulty in implementing the present results in laboratory experiments might arise when the texture of the hydrophobic surfaces is not smooth enough due to asperities of the order of the slip length (Choi & Kim 2006). However, the limitation of the present work in accurately predicting the hydrodynamic interaction for narrow channels ($H < 4$) or near rough surfaces may be surpassed by performing a full-scale computational fluid dynamics analysis in the future. Additionally, considering non-hydrodynamic interaction with the confinements (Jones *et al.* 2021), thermal fluctuation (Qian *et al.* 2013; Bregulla, Yang & Cichos 2014) and complex rheology of several biofluid media (Li & Xuan 2018; Zaferani, Suarez & Abbaspourrad 2021), researchers can develop more realistic models that better reflect the challenges that microswimmers might encounter in practical environments.

Funding. A.P. would like to acknowledge the support of the Department of Science and Technology, Government of India, through the project DST(SERB)(346)/2022-2023/940/MECH (grant no. SRG/2022/000416).

Declaration of interests. The authors report no conflict of interest.

Author ORCIDs.
Soumyajit Ghosh https://orcid.org/0009-0004-9892-0565;
Antarip Poddar https://orcid.org/0000-0001-7364-2942.

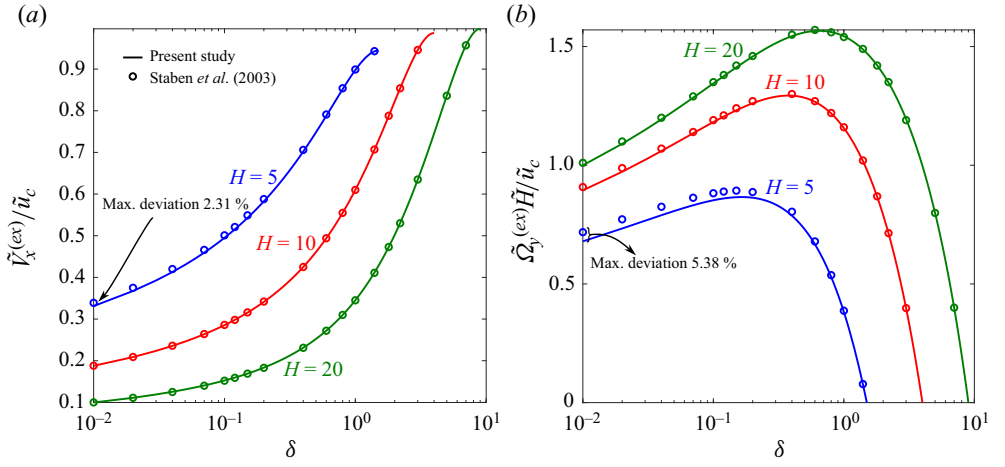

Figure 18. Variation of the translational and rotational velocities under the sole influence of the external plane Poiseuille flow.

Appendix A. Validity of superposition method

Figure 18 compares the translational and rotational velocity components obtained from the superposition method with the results obtained from Staben *et al.* (2003) for $H = 5$, 10 and 20. Hence, the selected channel height ($H = 6$) is within the valid range of the superposition approximation.

References

DE ÁVILA, B.E.-F., *et al.*2017 Micromotor-enabled active drug delivery for *in vivo* treatment of stomach infection. *Nat. Commun.* **8** (1), 272.

BAKER, R., *et al.*2019 Fight the flow: the role of shear in artificial rheotaxis for individual and collective motion. *Nanoscale* **11** (22), 10944–10951.

BARABAN, L., HARAZIM, S.M., SANCHEZ, S. & SCHMIDT, O.G. 2013 Chemotactic behavior of catalytic motors in microfluidic channels. *Angew. Chem.* **125** (21), 5662–5666.

BARRY, M.T., RUSCONI, R., GUASTO, J.S. & STOCKER, R. 2015 Shear-induced orientational dynamics and spatial heterogeneity in suspensions of motile phytoplankton. *J. R. Soc. Interface* **12** (112), 20150791.

BEHERA, N., PODDAR, A. & CHAKRABORTY, S. 2023 Eccentricity-induced dielectrophoretic migration of a compound drop in a uniform external electric field. *J. Fluid Mech.* **963**, A17.

BERKE, A.P., TURNER, L., BERG, H.C. & LAUGA, E. 2008 Hydrodynamic attraction of swimming microorganisms by surfaces. *Phys. Rev. Lett.* **101** (3), 038102.

BLAKE, J.R. 1971 A spherical envelope approach to ciliary propulsion. *J. Fluid Mech.* **46** (1), 199–208.

BREGULLA, A.P., YANG, H. & CICHOS, F. 2014 Stochastic localization of microswimmers by photon nudging. *ACS Nano* **8** (7), 6542–6550.

BRETHERTON, F. & ROTHSCHILD, N.M.V. 1961 Rheotaxis of spermatozoa. *Proc. R. Soc. Lond.* B*: Biol. Sci.* **153** (953), 490–502.

BROSSEAU, Q., USABIAGA, F.B., LUSHI, E., WU, Y., RISTROPH, L., ZHANG, J., WARD, M. & SHELLEY, M.J. 2019 Relating rheotaxis and hydrodynamic actuation using asymmetric gold–platinum phoretic rods. *Phys. Rev. Lett.* **123** (17), 178004.

CHAKRABORTY, S. 2008 Generalization of interfacial electrohydrodynamics in the presence of hydrophobic interactions in narrow fluidic confinements. *Phys. Rev. Lett.* **100** (9), 097801.

CHAPRA, S.C. 2010 *Numerical Methods for Engineers*. McGraw-Hill.

CHOI, C.-H. & KIM, C.-J. 2006 Large slip of aqueous liquid flow over a nanoengineered superhydrophobic surface. *Phys. Rev. Lett.* **96** (6), 066001.

CHOUDHARY, A., PAUL, S., RÜHLE, F. & STARK, H. 2022 How inertial lift affects the dynamics of a microswimmer in Poiseuille flow. *Commun. Phys.* **5** (1), 14.

CHOUDHARY, A. & STARK, H. 2022 On the cross-streamline lift of microswimmers in viscoelastic flows. *Soft Matt.* **18** (1), 48–52.
COSSON, J., HUITOREL, P. & GAGNON, C. 2003 How spermatozoa come to be confined to surfaces. *Cell Motil. Cytoskel.* **54** (1), 56–63.
DAMOR, H., GHOSH, S. & PODDAR, A. 2023 Surface entrapment of micromotors by a background temperature field. *Phys. Fluids* **35** (8), 082008.
DEY, R., BUNESS, C.M., HOKMABAD, B.V., JIN, C. & MAASS, C.C. 2022 Oscillatory rheotaxis of artificial swimmers in microchannels. *Nat. Commun.* **13** (1), 2952.
DI LEONARDO, R., DELL'ARCIPRETE, D., ANGELANI, L. & IEBBA, V. 2011 Swimming with an image. *Phys. Rev. Lett.* **106** (3), 038101.
DRESCHER, K., DUNKEL, J., CISNEROS, L.H., GANGULY, S. & GOLDSTEIN, R.E. 2011 Fluid dynamics and noise in bacterial cell–cell and cell–surface scattering. *Proc. Natl Acad. Sci.* **108** (27), 10940–10945.
ELGETI, J., WINKLER, R.G. & GOMPPER, G. 2015 Physics of microswimmers – single particle motion and collective behavior: a review. *Rep. Prog. Phys.* **78** (5), 056601.
FISCHER, P. 2018 A machine from machines. *Nat. Phys.* **14** (11), 1072–1073.
GENTILI, D., BOLOGNESI, G., GIACOMELLO, A., CHINAPPI, M. & CASCIOLA, C. 2014 Pressure effects on water slippage over silane-coated rough surfaces: pillars and holes. *Microfluid Nanofluid* **16**, 1009–1018.
GHALYA, N., SELLIER, A., EKIEL-JEŻEWSKA, M.L. & FEUILLEBOIS, F. 2020 Effective viscosity of a dilute homogeneous suspension of spheres in Poiseuille flow between parallel slip walls. *J. Fluid Mech.* **899**, A13.
GHOSH, S. & PODDAR, A. 2023 Slippery rheotaxis: new regimes for guiding wall-bound microswimmers. *J. Fluid Mech.* **967**, A14.
GUIDOBALDI, H.A., JEYARAM, Y., CONDAT, C., OVIEDO, M., BERDAKIN, I., MOSHCHALKOV, V., GIOJALAS, L.C., SILHANEK, A. & MARCONI, V.I. 2015 Disrupting the wall accumulation of human sperm cells by artificial corrugation. *Biomicrofluidics* **9** (2), 024122.
HAN, K., SHIELDS, C.W. IV & Velev, O.D. 2018 Engineering of self-propelling microbots and microdevices powered by magnetic and electric fields. *Adv. Funct. Mater.* **28** (25), 1705953.
HILL, J., KALKANCI, O., MCMURRY, J.L. & KOSER, H. 2007 Hydrodynamic surface interactions enable *Escherichia coli* to seek efficient routes to swim upstream. *Phys. Rev. Lett.* **98** (6), 068101.
HO, B. & LEAL, L. 1974 Inertial migration of rigid spheres in two-dimensional unidirectional flows. *J. Fluid Mech.* **65** (2), 365–400.
HU, J., WYSOCKI, A., WINKLER, R.G. & GOMPPER, G. 2015 Physical sensing of surface properties by microswimmers – directing bacterial motion via wall slip. *Sci. Rep.* **5** (1), 9586.
HUANG, J., CHEN, H., LI, N. & ZHAO, Y. 2023 Emerging microfluidic technologies for sperm sorting. *Eng. Regen.* **4**, 161–169.
HUFFNAGLE, G., DICKSON, R. & LUKACS, N. 2017 The respiratory tract microbiome and lung inflammation: a two-way street. *Mucosal Immunol.* **10** (2), 299–306.
ISHIKAWA, T., SIMMONDS, M.P. & PEDLEY, T.J. 2006 Hydrodynamic interaction of two swimming model micro-organisms. *J. Fluid Mech.* **568**, 119–160.
ISHIMOTO, K. 2017 Guidance of microswimmers by wall and flow: thigmotaxis and rheotaxis of unsteady squirmers in two and three dimensions. *Phys. Rev.* E **96** (4), 043103.
ISHIMOTO, K. & GAFFNEY, E.A. 2013 Squirmer dynamics near a boundary. *Phys. Rev.* E **88** (6), 062702.
JANA, S., UM, S.H. & JUNG, S. 2012 *Paramecium* swimming in capillary tube. *Phys. Fluids* **24** (4), 041901.
JONES, C., GOMEZ, M., MUOIO, R.M., VIDAL, A., MCKNIGHT, R.A., BRUBAKER, N.D. & AHMED, W.W. 2021 Stochastic force dynamics of the model microswimmer *Chlamydomonas reinhardtii*: active forces and energetics. *Phys. Rev.* E **103** (3), 032403.
JONES, R. 2004 Spherical particle in Poiseuille flow between planar walls. *J. Chem. Phys.* **121** (1), 483–500.
JUNOT, G., FIGUEROA-MORALES, N., DARNIGE, T., LINDNER, A., SOTO, R., AURADOU, H. & CLÉMENT, E. 2019 Swimming bacteria in Poiseuille flow: the quest for active Bretherton–Jeffery trajectories. *Europhys. Lett.* **126** (4), 44003.
KANTSLER, V., DUNKEL, J., BLAYNEY, M. & GOLDSTEIN, R.E. 2014 Rheotaxis facilitates upstream navigation of mammalian sperm cells. *Elife* **3**, e02403.
KANTSLER, V., DUNKEL, J., POLIN, M. & GOLDSTEIN, R.E. 2013 Ciliary contact interactions dominate surface scattering of swimming eukaryotes. *Proc. Natl Acad. Sci.* **110** (4), 1187–1192.
KATURI, J., USPAL, W.E., SIMMCHEN, J., MIGUEL-LÓPEZ, A. & SÁNCHEZ, S. 2018 Cross-stream migration of active particles. *Sci. Adv.* **4** (1), eaao1755.
KAYA, T. & KOSER, H. 2012 Direct upstream motility in *Escherichia coli*. *Biophys. J.* **102** (7), 1514–1523.
KIM, S. & KARRILA, S.J. 2013 *Microhydrodynamics: Principles and Selected Applications*. Courier Corporation.

KUMAR, M. & ARDEKANI, A.M. 2019 Effect of external shear flow on sperm motility. *Soft Matt.* **15** (31), 6269–6277.

KUZNETSOV, Y.A. 1998 *Elements of Applied Bifurcation Theory*, 2nd edn. Springer.

LAUGA, E., BRENNER, M.P. & STONE, H.A. 2005 Microfluidics: the no-slip boundary condition. arXiv.cond-mat/0501557.

LAUGA, E., DILUZIO, W.R., WHITESIDES, G.M. & STONE, H.A. 2006 Swimming in circles: motion of bacteria near solid boundaries. *Biophys. J.* **90** (2), 400–412.

LAUGA, E. & POWERS, T.R. 2009 The hydrodynamics of swimming microorganisms. *Rep. Prog. Phys.* **72** (9), 096601.

LEE, S. & LEAL, L. 1980 Motion of a sphere in the presence of a plane interface. Part 2. An exact solution in bipolar co-ordinates. *J. Fluid Mech.* **98** (1), 193–224.

LEMELLE, L., PALIERNE, J.-F., CHATRE, E., VAILLANT, C. & PLACE, C. 2013 Curvature reversal of the circular motion of swimming bacteria probes for slip at solid/liquid interfaces. *Soft Matt.* **9** (41), 9759–9762.

LI, D. & XUAN, X. 2018 Electrophoretic slip-tuned particle migration in microchannel viscoelastic fluid flows. *Phys. Rev. Fluids* **3** (7), 074202.

LI, G. & TANG, J.X. 2009 Accumulation of microswimmers near a surface mediated by collision and rotational Brownian motion. *Phys. Rev. Lett.* **103** (7), 078101.

LI, G.-J. & ARDEKANI, A.M. 2014 Hydrodynamic interaction of microswimmers near a wall. *Phys. Rev.* E **90** (1), 013010.

LIGHTHILL, M.J. 1952 On the squirming motion of nearly spherical deformable bodies through liquids at very small Reynolds numbers. *Commun. Pure Appl. Math.* **5** (2), 109–118.

LIMA, A.C. & MANO, J.F. 2015 Micro-/nano-structured superhydrophobic surfaces in the biomedical field. Part I. Basic concepts and biomimetic approaches. *Nanomedicine* **10** (1), 103–119.

LOPEZ, D. & LAUGA, E. 2014 Dynamics of swimming bacteria at complex interfaces. *Phys. Fluids* **26** (7), 071902.

MANTRIPRAGADA, V.T. & PODDAR, A. 2022 Rheology dictated spreading regimes of a non-isothermal sessile drop. *J. Fluid Mech.* **951**, A42.

MARCOS, FU, H.C., POWERS, T.R. & STOCKER, R. 2012 Bacterial rheotaxis. *Proc. Natl Acad. Sci.* **109** (13), 4780–4785.

MATHIJSSEN, A.J., DOOSTMOHAMMADI, A., YEOMANS, J.M. & SHENDRUK, T.N. 2016 Hydrodynamics of micro-swimmers in films. *J. Fluid Mech.* **806**, 35–70.

MATHIJSSEN, A.J., PUSHKIN, D.O. & YEOMANS, J.M. 2015 Tracer trajectories and displacement due to a micro-swimmer near a surface. *J. Fluid Mech.* **773**, 498–519.

MIKI, K. & CLAPHAM, D.E. 2013 Rheotaxis guides mammalian sperm. *Curr. Biol.* **23** (6), 443–452.

MOLAEI, M., BARRY, M., STOCKER, R. & SHENG, J. 2014 Failed escape: solid surfaces prevent tumbling of *Escherichia coli*. *Phys. Rev. Lett.* **113** (6), 068103.

NATH, B., CAPRINI, L., MAGGI, C., ZIZZARI, A., ARIMA, V., VIOLA, I., DI LEONARDO, R. & PUGLISI, A. 2023 A microfluidic method for passive trapping of sperms in microstructures. *Lab on a Chip* **23** (4), 773–784.

NAVIER, C. 1823 Mémoire sur les lois du mouvement des fluides. In *Mémoire de l'Académie Royale des Siences de l'Institut de France*, vol. VI, pp. 389–440. Sciences de L'Institut de France.

OMORI, T., KIKUCHI, K., SCHMITZ, M., PAVLOVIC, M., CHUANG, C.-H. & ISHIKAWA, T. 2022 Rheotaxis and migration of an unsteady microswimmer. *J. Fluid Mech.* **930**, A30.

PALACCI, J., SACANNA, S., ABRAMIAN, A., BARRAL, J., HANSON, K., GROSBERG, A.Y., PINE, D.J. & CHAIKIN, P.M. 2015 Artificial rheotaxis. *Sci. Adv.* **1** (4), e1400214.

PASOL, L., MARTIN, M., EKIEL-JEŻEWSKA, M., WAJNRYB, E., BŁAWZDZIEWICZ, J. & FEUILLEBOIS, F. 2011 Motion of a sphere parallel to plane walls in a Poiseuille flow: application to field-flow fractionation and hydrodynamic chromatography. *Chem. Engng Sci.* **66** (18), 4078–4089.

PIMPONI, D., CHINAPPI, M., GUALTIERI, P. & CASCIOLA, C.M. 2016 Hydrodynamics of flagellated microswimmers near free-slip interfaces. *J. Fluid Mech.* **789**, 514–533.

PODDAR, A. 2023 Thermotactic navigation of an artificial microswimmer near a plane wall. *J. Fluid Mech.* **956**, A25.

PODDAR, A., BANDOPADHYAY, A. & CHAKRABORTY, S. 2019*a* Activated micromotor propulsion by enzyme catalysis in a biofluid medium. *Appl. Phys. Lett.* **114** (5), 053701.

PODDAR, A., BANDOPADHYAY, A. & CHAKRABORTY, S. 2020 Near-wall hydrodynamic slip triggers swimming state transition of micro-organisms. *J. Fluid Mech.* **894**, A11.

PODDAR, A., BANDOPADHYAY, A. & CHAKRABORTY, S. 2021 Steering a thermally activated micromotor with a nearby isothermal wall. *J. Fluid Mech.* **915**, A22.

PODDAR, A., MANDAL, S., BANDOPADHYAY, A. & CHAKRABORTY, S. 2018 Sedimentation of a surfactant-laden drop under the influence of an electric field. *J. Fluid Mech.* **849**, 277–311.

PODDAR, A., MANDAL, S., BANDOPADHYAY, A. & CHAKRABORTY, S. 2019*b* Electrorheology of a dilute emulsion of surfactant-covered drops. *J. Fluid Mech.* **881**, 524–550.

QIAN, B., MONTIEL, D., BREGULLA, A., CICHOS, F. & YANG, H. 2013 Harnessing thermal fluctuations for purposeful activities: the manipulation of single micro-swimmers by adaptive photon nudging. *Chem. Sci.* **4** (4), 1420–1429.

REN, L., ZHOU, D., MAO, Z., XU, P., HUANG, T.J. & MALLOUK, T.E. 2017 Rheotaxis of bimetallic micromotors driven by chemical–acoustic hybrid power. *ACS Nano* **11** (10), 10591–10598.

ROTHSCHILD 1963 Non-random distribution of bull spermatozoa in a drop of sperm suspension. *Nature* **198** (4886), 1221–1222.

RUSCONI, R., GUASTO, J.S. & STOCKER, R. 2014 Bacterial transport suppressed by fluid shear. *Nat. Phys.* **10** (3), 212–217.

SCHAAR, K., ZÖTTL, A. & STARK, H. 2015 Detention times of microswimmers close to surfaces: influence of hydrodynamic interactions and noise. *Phys. Rev. Lett.* **115** (3), 038101.

SHAIK, V.A. & ARDEKANI, A.M. 2017 Motion of a model swimmer near a weakly deforming interface. *J. Fluid Mech.* **824**, 42–73.

SHARAN, P., XIAO, Z., MANCUSO, V., USPAL, W.E. & SIMMCHEN, J. 2022 Upstream rheotaxis of catalytic Janus spheres. *ACS Nano* **16** (3), 4599–4608.

SHUM, H., GAFFNEY, E.A. & SMITH, D.J. 2010 Modelling bacterial behaviour close to a no-slip plane boundary: the influence of bacterial geometry. *Proc. R. Soc. A: Math. Phys. Engng Sci.* **466** (2118), 1725–1748.

SPAGNOLIE, S.E. & LAUGA, E. 2012 Hydrodynamics of self-propulsion near a boundary: predictions and accuracy of far-field approximations. *J. Fluid Mech.* **700**, 105–147.

STABEN, M.E., ZINCHENKO, A.Z. & DAVIS, R.H. 2003 Motion of a particle between two parallel plane walls in low-Reynolds-number Poiseuille flow. *Phys. Fluids* **15** (6), 1711–1733.

STARK, H. 2016 Swimming in external fields. *Eur. Phys. J. Spec. Top.* **225**, 2369–2387.

TOTTORI, S. & NELSON, B.J. 2018 Controlled propulsion of two-dimensional microswimmers in a precessing magnetic field. *Small* **14** (24), 1800722.

TRETHEWAY, D.C. & MEINHART, C.D. 2004 A generating mechanism for apparent fluid slip in hydrophobic microchannels. *Phys. Fluids* **16** (5), 1509–1515.

USPAL, W., POPESCU, M.N., DIETRICH, S. & TASINKEVYCH, M. 2015 Rheotaxis of spherical active particles near a planar wall. *Soft Matt.* **11** (33), 6613–6632.

VEGA-SÁNCHEZ, C. & NETO, C. 2022 Pressure drop measurements in microfluidic devices: a review on the accurate quantification of interfacial slip. *Adv. Mater. Interfaces* **9** (5), 2101641.

WALKER, B.J., WHEELER, R.J., ISHIMOTO, K. & GAFFNEY, E.A. 2019 Boundary behaviours of *Leishmania mexicana*: a hydrodynamic simulation study. *J. Theor. Biol.* **462**, 311–320.

WANG, S., RYU, J., HE, G.-Q., QIN, F. & SUNG, H.J. 2020 A self-propelled flexible plate with a Navier slip surface. *Phys. Fluids* **32** (2), 021906.

ZAFERANI, M., SUAREZ, S.S. & ABBASPOURRAD, A. 2021 Mammalian sperm hyperactivation regulates navigation via physical boundaries and promotes pseudo-chemotaxis. *Proc. Natl Acad. Sci.* **118** (44), e2107500118.

ZHOU, T., WAN, X., HUANG, D.Z., LI, Z., PENG, Z., ANANDKUMAR, A., BRADY, J.F., STERNBERG, P.W. & DARAIO, C. 2024 AI-aided geometric design of anti-infection catheters. *Sci. Adv.* **10** (1), eadj1741.

ZHU, L., LAUGA, E. & BRANDT, L. 2013 Low-Reynolds-number swimming in a capillary tube. *J. Fluid Mech.* **726**, 285–311.

ZÖTTL, A. 2014 Hydrodynamics of microswimmers in confinement and in Poiseuille flow. PhD thesis, Technische Universität, Berlin.

ZÖTTL, A. & STARK, H. 2012 Nonlinear dynamics of a microswimmer in Poiseuille flow. *Phys. Rev. Lett.* **108** (21), 218104.